nature communications



Article

https://doi.org/10.1038/s41467-024-50709-y

Confining platinum clusters in indiummodified ZSM-5 zeolite to promote propane dehydrogenation

Received: 1 January 2024

Accepted: 15 July 2024

Published online: 02 August 2024

Check for updates

Yong Yuan^{1,4}, Erwei Huang^{1,4}, Sooyeon Hwang ¹², Ping Liu ≥ & Jingguang G. Chen ^{1,3} □

Designing highly active and stable catalytic sites is often challenging due to the complex synthesis procedure and the agglomeration of active sites during high-temperature reactions. Here, we report a facile two-step method to synthesize Pt clusters confined by In-modified ZSM-5 zeolite. In-situ characterization confirms that In is located at the extra-framework position of ZSM-5 as In⁺, and the Pt clusters are stabilized by the In-ZSM-5 zeolite. The resulting Pt clusters confined in In-ZSM-5 show excellent propane conversion, propylene selectivity, and catalytic stability, outperforming monometallic Pt, In, and bimetallic PtIn alloys. The incorporation of In⁺ in ZSM-5 neutralizes Brønsted acid sites to inhibit side reactions, as well as tunes the electronic properties of Pt clusters to facilitate propane activation and propylene desorption. The strategy of combining precious metal clusters with metal cation-exchanged zeolites opens the avenue to develop stable heterogeneous catalysts for other reaction systems.

The influence of the size of metal particles is critically important in heterogeneous catalysis, as it directly impacts catalytic rates, product selectivity, and catalyst durability¹⁻³. Typically, smaller active centers, including single atoms and clusters, often demonstrate superior performance compared to larger metal nanoparticles¹. This is due to their enhanced metal utilization efficiency, potential to increase intrinsic catalytic rates, and ability to reduce side reactions¹. Despite these advantages, maintaining the stability of these small active species presents a significant challenge. They are prone to agglomerating into nanoparticles, especially during high-temperature processes such as propane dehydrogenation (PDH)⁴. Consequently, developing efficient and economical methods to synthesize and stabilize these small active sites remains to be a topic of significant interest⁵⁻⁸.

PDH is one of the most important on-purpose propylene production technologies. It has gained significant attention in both academia and industry due to its high propylene selectivity and atom economy compared to traditional petroleum-based processes such as catalytic cracking and steam cracking⁹⁻¹¹. The abundance of shale gas-

derived propane has made PDH even more essential to meet the growing demand for propylene¹²⁻¹⁴. Currently, commercial Oleflex and Catofin processes utilize Pt- and CrO_x-based catalysts, respectively⁴. Although numerous potential PDH catalysts such as GaO_x, VO_x¹⁵, $ZrO_x^{16,17}$, and $ZrO_x^{4,11,18}$ have been reported, Pt-based catalysts are extensively investigated for their superior C-H dissociation ability compared to other catalysts. Recent studies have demonstrated that single Pt atoms or clusters can provide better turnover frequency and propylene selectivity^{19,20}. Meanwhile, side reactions such as hydrogenolysis and coke deposition are structure-sensitive and are influenced by the size of Pt nanoparticles. To improve the PDH performance of Pt-based catalysts, the addition of a second metal component has been explored, such as Sn, Zn, Mn, Ga, or Cu^{10,11,21-23}. This approach is efficient in separating Pt ensembles, forming Pt-M alloy²¹, Pt-M intermetallic^{24,25}, or single atom alloy²⁶ catalysts. However, it has been shown that the alloy-free Pt species shows better intrinsic dehydrogenation ability, although it exhibits poor stability^{5,27}. To achieve highly active and stable Pt sites for PDH, one strategy is to

confine Pt species by metal-modified zeolites, which are commercially available and therefore facilitate scaling up possibilities.

Zeolites have garnered attention for PDH owing to the advantageous confinement provided by their structures^{6,27-29}. For example, Corma and coworkers have developed a one-pot synthesis of PtSn clusters encapsulated in the ZSM-5 zeolite^{28,29}, exhibiting high propylene selectivity and PDH activity. Qi et al.6 have synthesized Znmodified dealuminated Beta zeolite catalyst and integrated Pt atoms to form PtZn₍₄₋₆₎ sites, showing high PDH activity, propylene selectivity, and catalyst stability. It is worth noting that the siliceous or germanium zeolites are frequently used over Al-containing zeolites^{5,30}. This preference is due to Al-containing zeolites having Brønsted acid sites (BASs) that catalyze undesirable side reactions, including propane cracking, oligomerization, and aromatization, consequently decreasing propylene selectivity31. While Al-free zeolites can be obtained either via direct zeolite synthesis without Al precursors or through the dealumination of Al-containing zeolites, both methodologies pose challenges: they involve costly precursors, complex preparation steps, and are limited to certain zeolite types^{27,29,30,32-34}. Recently, it was reported RhIn@MFI exhibited superior stability for propane dehydrogenation³⁴. The preparation process involved the synthesis of Rh@MFI through the hydrothermal method, followed by the introduction of indium via impregnation. During the reaction, indium species migrated into the pores to form RhIn₄ clusters with stable propane dehydrogenation performance. Therefore, although the mobility of indium in reductive environments has been recognized by the research community as a significant strategy for synthesizing bimetallic catalysts, the reported zeolite-encapsulated bimetallic catalysts include at least one step involving hydrothermal synthesis. These factors may hinder scalability and commercial viability. The direct application of commercial Al-containing zeolites and only the impregnation method has not been reported, which is the subject of the current study. On the other hand, metal cation-exchanged zeolites (metal including Ga, Co, Zn, etc.) have also attracted attention for PDH³⁵⁻³⁹. Although these metal cation species show lower activity compared to Pt-based catalysts, replacing BAS with metal cations turns metal-zeolites into ideal hosts for confining Pt species. This could lead to the formation of Pt_x-M species at the extra-framework position in zeolites. Such synergy may create a novel type of active center, distinct from traditional PtM bimetallic configurations, and potentially enhance PDH performance.

Herein, we have developed a two-step method to synthesize Pt clusters confined by In-modified ZSM-5 zeolite. The process involves introducing In in H-ZSM-5 through the incipient wetness impregnation (IWI) method and calcination, followed by reduction to form In⁺ at the extra-framework position of ZSM-5 zeolites. In the second step, an appropriate amount of Pt is introduced in In-ZSM-5 using the same IWI method and calcination, resulting in Pt/In-ZSM-5 catalyst. In-situ characterization results have revealed that Pt clusters are slightly positively charged and In species are in the +1-oxidation state during propane dehydrogenation. The propane conversion over Pt/In-ZSM-5 was maintained at ~40% after 118 h and the propylene selectivity higher than 99.5%, representing a much better propane conversion compared to bulk PtIn alloys. To the best of our knowledge, this is the first time that commercial Al-containing zeolite has been directly used as anchoring sites to stabilize Pt species for PDH.

Results

Synthesis and characterization of In-ZSM-5 zeolite

A two-step method has been developed for preparing Pt/In-ZSM-5 catalyst: The first step involved exchanging In⁺ with BAS in the H-ZSM-5 zeolite, referred to as In-ZSM-5, and the second step introduced Pt into the In-ZSM-5 catalyst. The in-situ reduction of In/H-ZSM-5 resulted in the replacement of BAS by In⁺, known as the reductive solid-state ion-exchange process^{40,41}. As shown in Fig. 1a, upon dehydration, the diffuse reflectance infrared Fourier

transform spectroscopy (DRIFTS) results of In/H-ZSM-5 showed bands at 3735 and 3591 cm⁻¹, attributed to external silanol group (Si-OH) and bridge OH group associated with BAS⁴², respectively. Upon reduction at 550 °C, the BAS OH group disappeared, indicating the exchange of BAS with In. The difference spectra of before and after reduction confirmed the consumption of the BAS OH group (Fig. 1a). In-situ Fourier transform infrared spectroscopy using pyridine as a probe molecule (pyridine-FTIR) was employed to monitor the density of BAS. As shown in Fig. 1b, pyridineadsorbed H-ZSM-5 showed three characteristic peaks: 1540, 1490, and 1455 cm⁻¹. The 1540 and 1455 cm⁻¹ features were associated with the protonated pyridinium ion corresponding to BAS and coordinatively adsorbed pyridine on the Lewis acid site (LAS), respectively, while 1490 cm⁻¹ was attributed to the combination of pyridine adsorbed on BAS and LAS⁴². There was a ~30% decrease in BAS intensity and a minor increase of LAS intensity on calcined In/ H-ZSM-5, likely due to the partial ion-exchange between In cations and BAS during the impregnation steps. Upon reduction, the pyridinium band decreased by ~70% compared to parent H-ZSM-5, in parallel with the appearance of pyridine adsorbed on LAS (1455 and 1446 cm⁻¹), attributed to the formation of exchanged In species. Note that although the partial ion-exchange occurred during the impregnation steps, the extent of exchange was no more than 30%. The H₂-reduction process was required to promote the migration of surface InOx nanoparticles to neutralize sufficient BAS and produce a large fraction of exchanged In sites.

The in-situ X-ray absorption near edge structure (XANES) investigation shed light on the oxidation state of reduced In in In/H-ZSM-5 catalyst (Fig. 1c). The In of the fresh In/H-ZSM-5 showed identical absorption energy with In₂O₃, indicating In being in the +3-oxidation state. Upon reduction, the In K-edge showed a decrease in absorption energy, but different from the In foil (Fig. 1c). There has been an ongoing debate regarding the origin of decreasing absorption energy in metal-zeolites such as Ga/H-ZSM-5 and In-CHA catalysts^{37,41,43-46}. It was unresolved whether this reduction was due to the formation of a hydride or a reduced In with a lower oxidation state. The H₂-D₂ exchange experiment on reduced In/H-ZSM-5 revealed the absence of In hydride at 550 °C, which was typically characterized by a band between 1600 and 2000 cm⁻¹ wavenumber range⁴¹, as shown in Supplementary Fig. 1. This suggested that In⁺ instead of In hydride was most likely the species upon reducing In/H-ZSM-5. In addition, the In/ H-ZSM-5 did not exhibit any additional scattering peaks in the extended X-ray absorption fine structure (EXAFS) spectrum (Fig. 1d), which was different from In₂O₃ and the In foil. This distinction became more pronounced when the In/Al ratio was decreased to 0.2, where the In K-edge EXAFS feature of the reduced catalyst disappeared entirely (see Supplementary Note 1, Supplementary Fig. 2). This phenomenon was likely attributed to the formation of extraframework In⁺ species. Through linear combination fitting, it was estimated that ~70% of In₂O₃ was reduced in the In/H-ZSM-5 sample with an In/Al ratio of 1.0. This correlated closely with the consumption of BAS, following stoichiometry where one indium atom replaced one BAS to form In⁺ species. The significant reduction in the EXAFS scattering peak for the reduced In/H-ZSM-5 aligned with findings reported for the disappearance of In K-edge features in In-CHA⁴¹, although the exact reason for the disappearance would need to be further investigated. Upon subsequent oxidation, In⁺ was transitioned to the +3oxidation state (Fig. 1d). Importantly, the EXAFS spectrum displayed the In-O feature in the first shell without the In-O-In feature in the second shell (Fig. 1d). This suggested that although In⁺ was oxidized to +3 upon contact with air, the In remained to be isolated at the extra-framework position within the micropores of zeolites. This was different from the initial In₂O₃ particles located at the external surface, which showed the In-O feature in both the first and second shell in the EXAFS spectrum (Fig. 1d). Likewise, XRD measurements

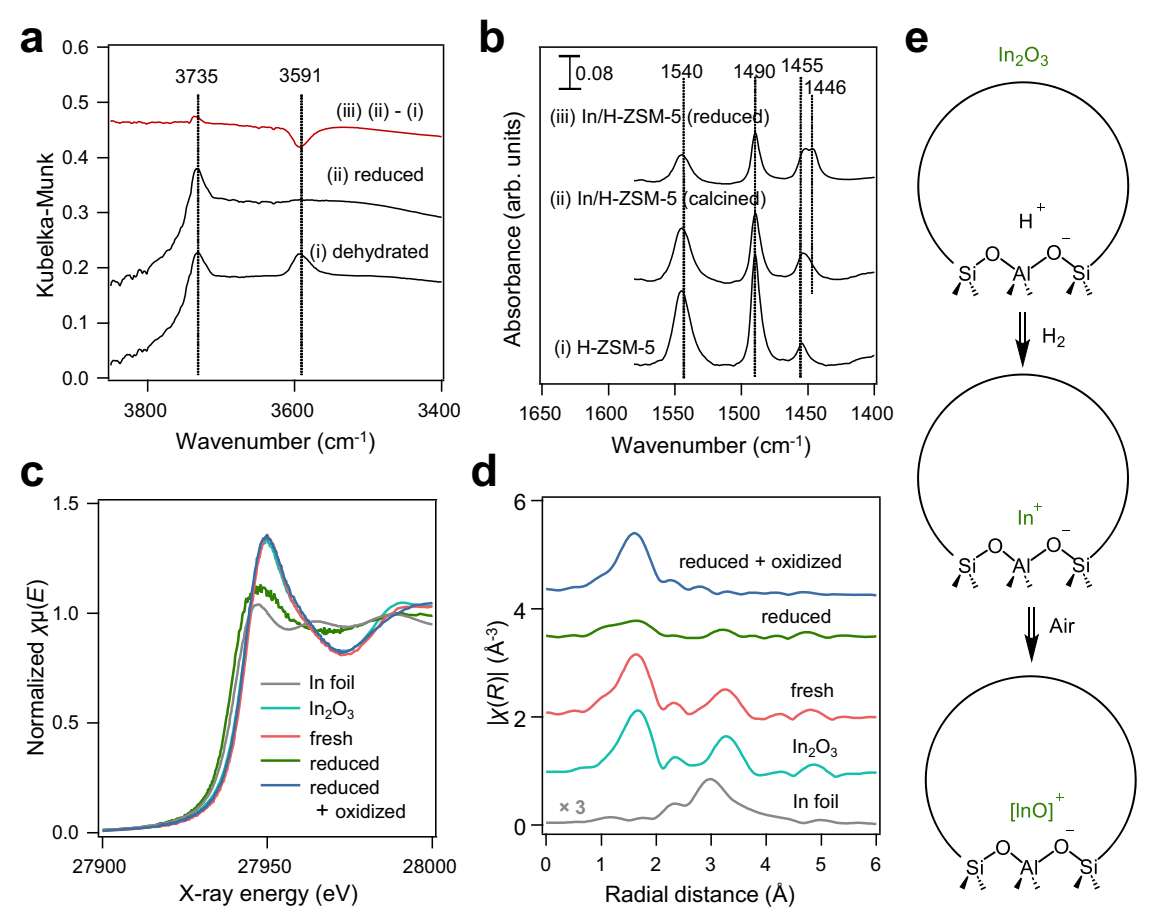


Fig. 1 | **Characterizations of In/H-ZSM-5 catalyst. a** In-situ DRIFTS spectra collected during reduction of In/H-ZSM-5: (i) dehydrated at 550 °C; (ii) reduced by 10 vol. % H₂/He at 550 °C; (iii) spectrum (i) subtracted from the spectrum (ii). **b** Pyridine-FTIR spectra of H-ZSM-5 and In/H-ZSM-5 with calcined and reduced conditions. The calcined sample was dehydrated at 550 °C before cooling to 150 °C for pyridine adsorption. The reduced condition represented that the sample was reduced at 550 °C before cooling to 150 °C for pyridine adsorption. **c** In-situ In K-edge XANES and (**d**) Fourier-transformed EXAFS spectra over In/H-ZSM-5 with

fresh and reduced conditions. The fresh catalyst referred to the calcined sample measured at room temperature. The reduced condition represented that the sample was reduced at 550 °C. The reduced + oxidized condition represented the sample was reduced at 550 °C and then oxidized by exposing the reduced indium species to the ambient atmosphere. In foil and $\ln_2 O_3$ were also measured as standards for reference. **e** Schematic of the reduction and subsequent oxidation of \ln/H -ZSM-5 catalyst.

(Supplementary Fig. 3) showed the crystalline In_2O_3 particles in the fresh In/H-ZSM-5 and disappeared upon reduction and subsequent oxidation by air, consistent with TEM images that In_2O_3 particles (-10 nm) observed on the fresh In/H-ZSM-5 catalyst nearly disappeared upon reduction (Supplementary Fig. 4).

The examination of In/Al ratios (Supplementary Figs. 2-8) revealed that as the In/Al ratio increased from 0.2 to 1.0, more BAS was replaced by In, but BAS could not be completely replaced even at a high In/Al ratio of 1.5. An excess of In led to the formation of unreduced InO_x oligomers. These observations suggested that at an In/Al ratio at or below 1.0, In+ was the dominant species upon reduction of In/H-ZSM-5 catalyst, and dispersed [InO]⁺ was the species when exposing the reduced indium species to the ambient atmosphere (Fig. 1e). In contrast, when indium was introduced onto siliceous MFI (Si-MFI) and SiO₂ supports, the indium oxide exhibited a higher reduction temperature (Supplementary Fig. 8), and furthermore, indium was unable to migrate into the micropores of Si-MFI (Supplementary Figs. 9, 10). This observation emphasized the critical role of BAS in H-ZSM-5, not only in facilitating the reduction of In₂O₃ but also in stabilizing the formation of extra-framework In⁺ ions. Using a traditional liquid ionexchange method, the In-ZSM-5(IE) zeolite attained an indium loading of only 0.8%, with an In/Al ratio of 0.17. TEM images (Supplementary Fig. 11) of the fresh and reduced In-ZSM-5(IE) showed the absence of indium oxide on the external surface, aligning with expectations from the ion-exchange process between indium species and BAS.

Propane dehydrogenation performance of Pt/In-ZSM-5 catalysts

Pt was introduced into In-ZSM-5 to prepare the Pt/In-ZSM-5 catalysts. For comparison, the same metal loadings were used to prepare Pt/H-ZSM-5, PtIn/H-ZSM-5 (one-step method) and PtIn/SiO₂. The propane (C₃H₈) dehydrogenation performance was tested with 20 vol% C₃H₈ in Ar at 550 °C. As shown in Fig. 2a, the Pt/In-ZSM-5 catalyst showed a stable propane conversion of ~48% without appreciable deactivation within 37 h. The propylene (C₃H₆) selectivity was higher than 99%. In comparison, Ptln/H-ZSM-5 and Ptln/SiO₂ showed much lower propane conversion, indicating that PtIn alloy formed on the external surface of H-ZSM- 5 and SiO₂ were less active than the PtIn species inside the micropores. In contrast, Pt/H-ZSM-5 showed a decreasing conversion over time on stream, although the initial propane conversion was higher than other catalysts. This was due to side reactions catalyzed by a large amount of BAS in Pt/H-ZSM-5 (Supplementary Fig. 12), which resulted in a lower propylene selectivity and carbon balance (Fig. 2b, d) compared to other catalysts. These BAS-catalyzed side reactions involved propane cracking, olefin oligomerization, and aromatization. Consequently, Pt/In-ZSM-5 delivered the highest propylene yield among these samples (Fig. 2c). Overall, Pt/In-ZSM-5 showed excellent

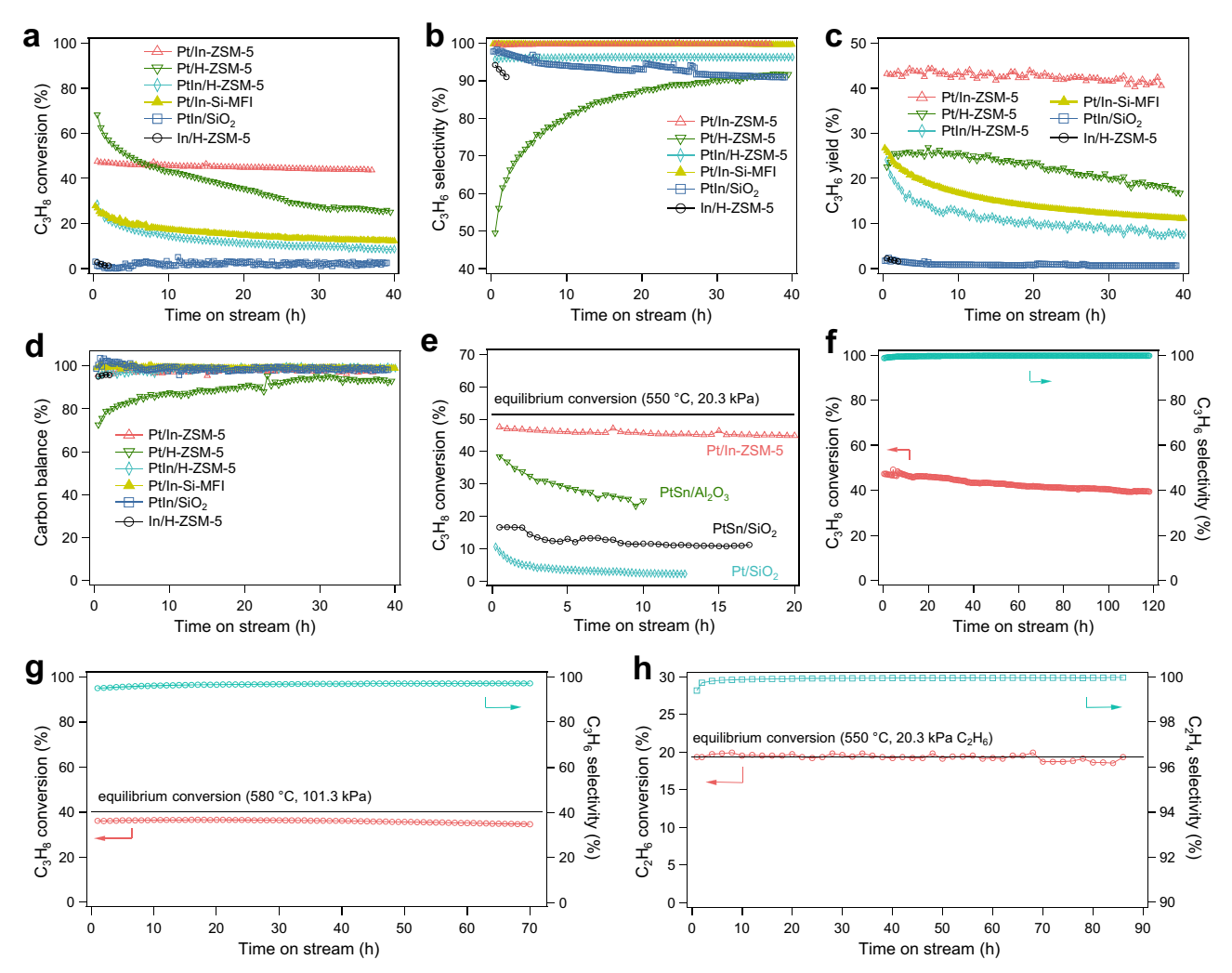


Fig. 2 | **Propane dehydrogenation performance of Pt/In-ZSM-5 catalyst. a** Propane conversion, **b** propylene selectivity, **c** propylene yield, and **d** carbon balance as a function of time on stream over Pt/In-ZSM-5 and control catalysts. **e** Comparison of propane conversion as a function of time on stream over Pt/In-ZSM-5 with PtSn/Al₂O₃, PtSn/SiO₂, and Pt/SiO₂ catalysts. **f** Propane dehydrogenation performance of Pt/In-ZSM-5 catalyst for long-term operation. Reaction

conditions of (**a**–**f**): 550 °C, pressure 20.3 kPa, and WHSV = 5.9 h⁻¹. **g** Propane dehydrogenation performance of Pt/In-ZSM-5 catalyst with an undiluted propane stream: 580 °C, pressure 101.3 kPa, and WHSV = 4.7 h⁻¹. **h** Ethane dehydrogenation performance: C_2H_6 conversion and C_2H_4 selectivity versus time on stream over Pt/In-ZSM-5 catalyst. Reaction conditions: 550 °C, pressure 20.3 kPa, and WHSV = 5.9 h⁻¹.

PDH performance in terms of propane conversion, propylene selectivity, and stability, outperforming other monometallic (Pt, In) and bimetallic (PtIn) with different combinations. Based on the control experiments shown here, In in the Pt/In-ZSM-5 catalyst had at least two roles: (1) neutralizing BAS to avoid side reactions; (2) stabilizing Pt species to serve as the highly active sites for PDH.

The PDH performance of Pt/In-ZSM-5 was compared with the benchmark PtSn-based catalysts using SiO₂ and Al₂O₃ as supports²⁴. As shown in Fig. 2e, both PtSn/Al₂O₃ and PtSn/SiO₂ showed much lower propane conversions than Pt/In-ZSM-5, although similar propylene selectivity and carbon balance were observed (Supplementary Fig. 13). In addition, as shown in Fig. 2f, the propane conversion over Pt/In-ZSM-5 maintained at -40% after 118 h and the propylene selectivity higher than 99.5%. The Pt/In-ZSM-5 catalyst was tested under 580 °C in the pure propane flow (WHSV = $4.7 \, h^{-1}$), as shown in Fig. 2g. Close to equilibrium conversion was obtained with a relatively minor deactivation with propane conversion from 36.2% to 34.7% while the propylene selectivity remained constant at 97.1% within 70 h. In addition, the catalytic performance of Pt/In-ZSM-5 was tested at increased weight hourly space velocities (WHSVs) of 39.3, 118, 236, and 531 h⁻¹ to obtain the C₃H₆ production rates and apparent rate coefficient. As shown in

Supplementary Fig. 14, at WHSVs of 118 h⁻¹ or higher, the C₃H₈ conversion was below 20%, with propylene selectivity exceeding 99.8%. The net C₃H₆ formation rates were calculated to be 49.1, 61.6, and 70.0 mol_{C3H6}·g_{Pt}⁻¹·h⁻¹ at WHSVs of 118, 236, and 531 h⁻¹, respectively. Considering that propane dehydrogenation was a reversible reaction, the forward apparent rate coefficient was derived based on the net C₃H₆ formation rates, inlet propane partial pressure, equilibrium constant, and propane conversion using the methodology provided in a previous study⁶. The apparent rate coefficient was determined to be $370 \text{ mol}_{\text{C3H6}} \cdot g_{\text{Pt}}^{-1} \cdot h^{-1} \cdot bar^{-1}$ at WHSV of $531 \, h^{-1}$. This value was higher than most of the reported PtGa-, PtZn-, PtIn-, and PtSn-based catalysts^{21,24,47,48}. Using ethane dehydrogenation as another probe reaction, Pt/In-ZSM-5 also showed equilibrium conversion for ethane dehydrogenation with a higher than 99% ethylene selectivity and no deactivation after 80 h (Fig. 2h). These results further confirmed the superior dehydrogenation abilities of the Pt/In-ZSM-5 catalyst.

The impact of the In/Al ratio of Pt/In-ZSM-5 catalysts was examined. As shown in Supplementary Fig. 15, as the In/Al ratio increased from 0.2 to 1.0, there was a decrease in the initial propane conversion, and an increase in propylene selectivity, propylene yield, and carbon balance. This was because more In⁺ neutralized more BAS, and thus led to fewer

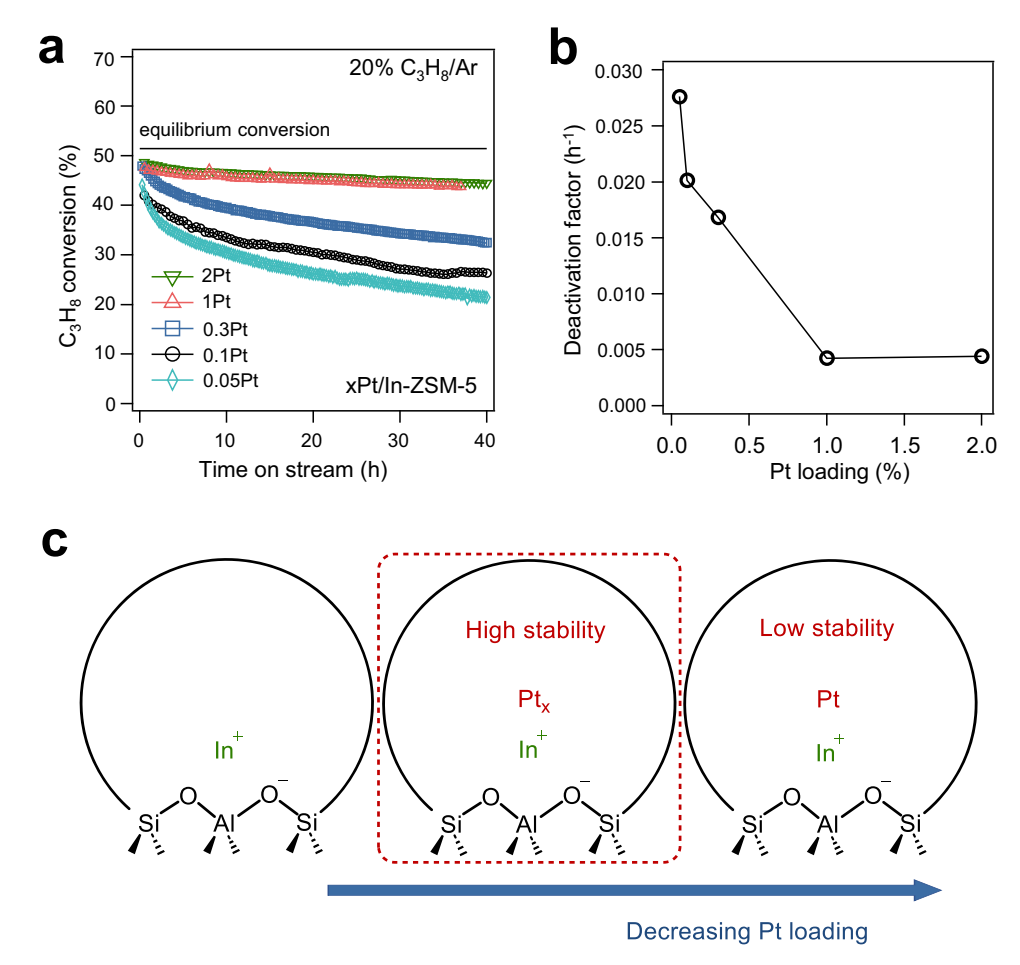


Fig. 3 | **Impact of Pt loading of the Pt/In-ZSM-5 catalysts on propane dehy-drogenation. a** Propane conversion over time on stream over Pt/In-ZSM-5 catalysts with different Pt loadings. **b** Deactivation coefficient of Pt/In-ZSM-5 catalysts with different Pt loadings. Note that the deactivation coefficient was determined within

37 h. Reaction conditions: 550 °C, pressure 20.3 kPa, and WHSV = $5.9\ h^{-1}$. c Schematic of the possible active species of Pt/In-ZSM-5 with dependence on Pt loading.

side reactions. On the other hand, an excess of In (In/Al = 1.5) was also detrimental to the PDH performance of Pt/In-ZSM-5 catalyst. The excess In₂O₃ could not diffuse into the micropores and located on the external surface as crystalline (Supplementary Figs. 3-8), which prevented the movement of Pt into the micropores of ZSM-5 and instead tended to form PtIn alloy on the external surface upon reduction. The resulting PtIn sites showed a similar performance to the case of PtIn/H-ZSM-5 and Ptln/SiO₂. Consequently, selecting the optimal In/Al ratio was crucial: the amount of indium should be sufficient to neutralize BAS without being excessive, yet too much indium would inhibit Pt from migrating into the micropores and instead promote the formation of PtIn alloy on the external surface. Through comparative studies of In-ZSM-5 and Pt/ In-ZSM-5 with various In/Al ratios, the optimal In/Al ratio was determined to be 1.0. The propane dehydrogenation performance of the Pt/ In-Si-MFI catalyst was also tested, as shown in Fig. 2a-d. Initially, the catalyst achieved approximately 30% propane conversion, but it gradually declined to ~10% within 40 h. This observation suggested that the PtIn species, likely forming a PtIn alloy, not only offered a relatively low propane conversion but also exhibited a fast deactivation within 40 h. Ptln/SiO₂ with different ratios (1:3 to 1:8) confirmed the poor propane dehydrogenation performance in terms of low propane conversion or fast deactivation (Fig. 2 and Supplementary Fig. 16). In addition, the prepared Pt/In-ZSM-5(IE) exhibited prominent deactivation, low propylene selectivity (Supplementary Fig. 17).

Employing the same method, Pt/Zn-ZSM-5, Pt/Ga-ZSM-5, and Pt/Co-ZSM-5 catalysts were synthesized to examine the influence of the

metal cation type. Supplementary Fig. 18 demonstrated a notable contrast with Pt/In-ZSM-5; the three new samples exhibited a decrease in propylene selectivity, although Pt/Zn-ZSM-5 and Pt/Ga-ZSM-5 showed higher propane conversions. As a result, Pt/In-ZSM-5 delivered the highest propylene yield. These results underscored the unique role of In in the Pt/M-ZSM-5 catalysts compared to other metal cations.

The influence of Pt loading in Pt/In-ZSM-5 catalysts on PDH was shown in Fig. 3a. Reducing Pt loading to as low as 0.05% led to a marginal decline in initial propane conversion. However, catalysts with lower Pt loading demonstrated deactivation over time on stream. As shown in Supplementary Fig. 19, catalysts with varying Pt loadings exhibited comparable high propylene selectivity. This similarity suggested that active sites, regardless of Pt loading, preferentially favored propylene desorption. The easy desorption of propylene likely prevented its further dehydrogenation on the surface, thereby ensuring high propylene selectivity²⁵. The catalyst deactivation was likely due to the instability of the active sites and the agglomeration at elevated temperatures (550 °C), which was usually a problem with single-atom catalysts¹. The deactivation coefficients for varying Pt loadings in Pt/In-ZSM-5 were presented in Fig. 3b. The deactivation coefficient of 1Pt/In-ZSM-5 was 0.0042 h⁻¹ within ~37 h, comparable to the value of 0.0038 h⁻¹ for PtSn/SiO₂ catalyst within 8 h and superior to other Pt-, Cr-, and Ga-based catalysts^{24,49}. It was hypothesized that reducing Pt loading from 1% to 0.05% changed Pt from clusters to single atoms; Pt clusters contributed to high propane conversion, propylene selectivity, and durable stability, whereas single Pt atoms exhibited poor

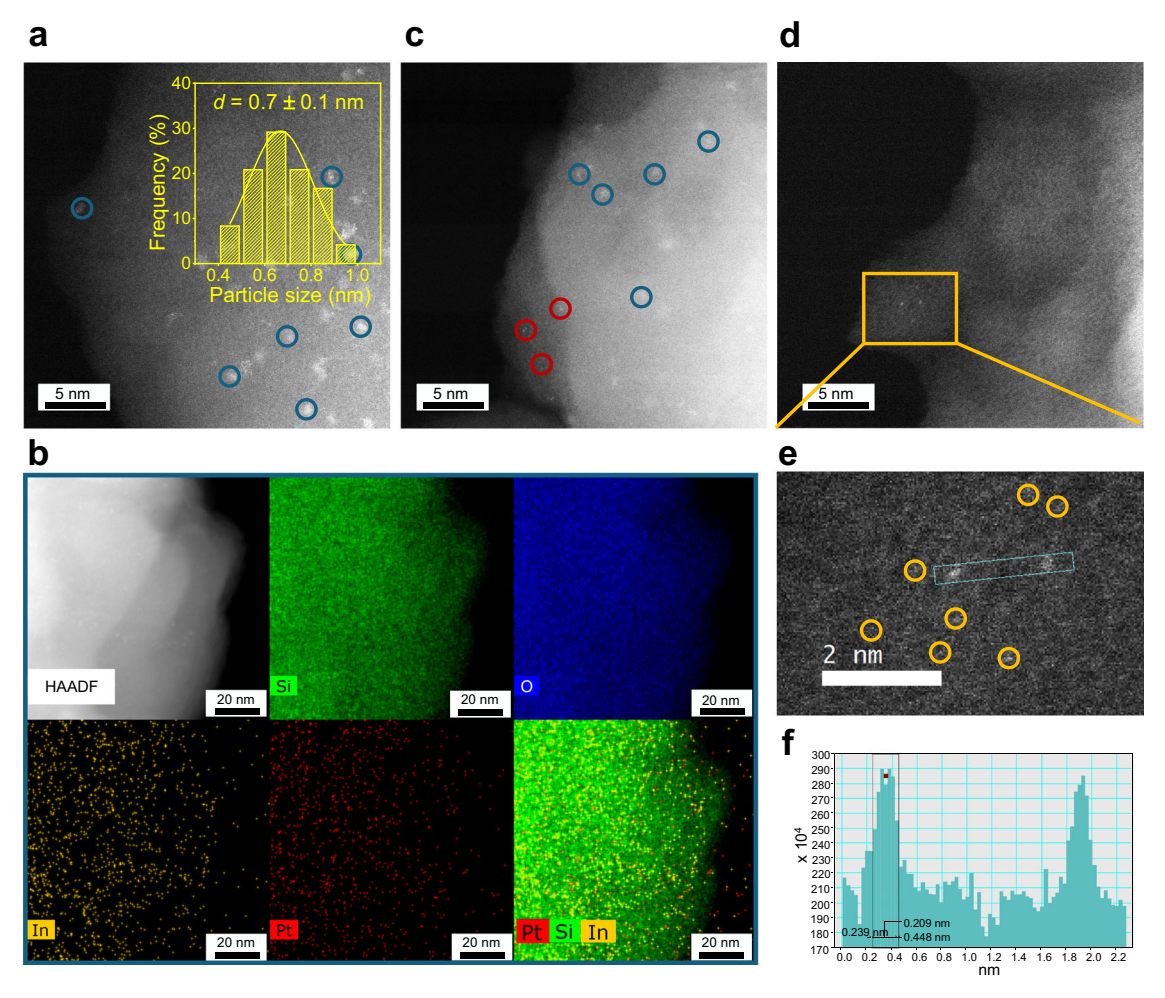


Fig. 4 | **HAADF-STEM analysis and STEM-EDS mapping of xPt/In-ZSM-5 catalysts upon reduction. a** HAADF-STEM image of 1Pt/In-ZSM-5. Inset in **(a)** showed the particle size distribution. **b** STEM-EDS mapping of 1Pt/In-ZSM-5. **c** HAADF-STEM image of 0.3Pt/In-ZSM-5. Red and blue circles in **(a)** and **(c)** showed the single Pt atom and Pt clusters, respectively. **d** HAADF-STEM image of 0.05Pt/In-ZSM-5. **e** A

zoomed-in image of the orange square in (**d**). Orange circles in (**e**) represented the less bright spots compared to the bright spots within the rectangular area. **f** Intensity profiles along the green area in (**e**). Note that the samples were reduced at 550 $^{\circ}$ C and then cooled down to room temperature before the TEM sample preparation.

stability, and were not promising from a practical application point of view (Fig. 3c).

The coke deposition on spent catalysts was investigated using Raman spectroscopy, temperature-programmed oxidation (TPO), and thermogravimetric analysis (TGA) (Supplementary Figs. 20–22). Notably, the Pt/In-ZSM-5 catalyst exhibited minimal carbon formation, significantly less than that observed on the Pt/H-ZSM-5 catalyst. In contrast, the 0.05Pt/In-ZSM-5 catalyst did not show carbon deposition, suggesting that deactivation resulted from the instability of isolated Pt atoms rather than coke deposition. TGA and TPO analysis further confirmed these observations. Based on this, the Pt/In-ZSM-5 catalyst under harsh conditions (600 °C in the pure propane flow) as well their regeneration ability was further evaluated (Supplementary Fig. 23). The results indicated a very slow deactivation rate over a period of 40 h. This minimal deactivation was attributed to coke formation at high temperatures. The produced coke could be easily regenerated through combustion, effectively restoring it to the original high performance.

Determination of active site in Pt/In-ZSM-5 catalysts

High-angle annular dark-field scanning transmission electron microscopy (HAADF-STEM) and energy-dispersive X-ray spectroscopy (STEM-EDS) were applied to analyze the reduced Pt/In-ZSM-5 catalysts, providing information about the size of Pt clusters. In the 1Pt/In-ZSM-5 catalyst, HAADF-STEM images revealed Pt clusters averaging 0.7 nm in

size (Fig. 4a). In contrast, 1Pt/H-ZSM-5 showed a larger particle size (1.3 nm, Supplementary Fig. 24) than 1Pt/In-ZSM-5 (0.7 nm), suggesting a confinement effect of In-ZSM-5. However, distinguishing between Pt and In elements was challenging due to insufficient contrast. STEM-EDS mapping of 1Pt/In-ZSM-5 (Fig. 4b) confirmed the even distribution of Pt and In within the catalyst. When the Pt loading was decreased to 0.3%, both Pt clusters and single Pt atoms were observed (Fig. 4c). At a lower Pt loading of 0.05%, HAADF-STEM images of 0.05Pt/In-ZSM-5 displayed only isolated Pt atoms (bright spots in Fig. 4d), with zoomedin areas showing these spots to be ~0.209 nm in diameter and wellseparated (Fig. 4e, f). Some less bright spots, potentially isolated In atoms or Pt atoms at varying thicknesses, were also noted (orange circles in Fig. 4e). Although distinguishing Pt from In atoms was difficult, the consistent In loadings across all three samples suggested that the bright spots in HAADF-STEM images should be Pt atoms. STEM-EDS mapping of 0.3Pt/In-ZSM-5 and 0.05Pt/In-ZSM-5 catalysts (Supplementary Figs. 25, 26) further supported the uniform distribution of Pt and In. These results indicated that at the Pt loading of 1%, Pt clusters were predominant, while at the low loading (0.05%), isolated Pt atoms were primarily present. HAADF-STEM images of 1Pt/In-ZSM-5 and 0.05Pt/In-ZSM-5 catalysts after PDH test showed that no particle growth was observed on 1Pt/In-ZSM-5, but isolated Pt atoms agglomerated on the 0.05 Pt/In-ZSM-5 catalyst (Supplementary Fig. 27). Correlating these findings with PDH performance (Figs. 2, 3) led to the

conclusion that Pt clusters played a crucial role in the observed superior PDH performance. HAADF-STEM analysis of the Pt/In-Si-MFI and Pt/In-ZSM-5(IE) after reaction revealed Pt with sizes of -1.2 nm and 1.3 nm, respectively, as shown in Supplementary Fig. 28, 29, similar to the observation of Pt in Pt/H-ZSM-5 catalyst. This indicated that the Pt species were predominantly located on the outer surface of the zeolites, rather than within the micropores. HAADF-STEM analysis of the spent PtIn/SiO₂ identified an average size of 3 nm (Supplementary Fig. 30). Moreover, while X-ray diffraction (XRD) measurements did not reveal any active site information for the Pt/In-ZSM-5 due to the small size of the species, the spent PtIn/SiO₂ showed PtIn₂ as the dominant phase (Supplementary Fig. 31).

In-situ X-ray absorption fine structure (XAFS) investigations were conducted to elucidate the active site of PtIn-based catalysts. For fresh samples, both Pt and In elements were predominantly in their oxidized forms (see Supplementary Fig. 32 and Supplementary Note 2 for detailed discussion). Upon reduction, as shown in Fig. 5, the In K-edge of all PtIn-related samples exhibited a decrease in absorption energy. Specifically, for Pt/In-ZSM-5 and PtIn/H-ZSM-5, the reduction-induced shift in the In K-edge absorption was similar to that observed in In/H-ZSM-5 catalysts (Supplementary Fig. 2 and Supplementary Note 1), showing a significant decrease in absorption energy, yet distinct from that of the In foil. A closer examination revealed that Pt/In-ZSM-5 exhibited a slightly greater decrease in absorption energy compared to In/H-ZSM-5 sample. This slight variance was attributed to the interaction between Pt species and In⁺. In the case of PtIn/H-ZSM-5, the presence of an excess amount of In species resulted in the formation of In+ species in the reduced samples, as confirmed by pyridine-FTIR results (Supplementary Fig. 12). Consequently, both Pt/In-ZSM-5 and PtIn/H-

ZSM-5 exhibited a nearly complete disappearance of EXAFS features at the In K-edge (Fig. 5b). A careful examination of the Fouriertransformed EXAFS spectra at the In K-edge of the Pt/In-ZSM-5 catalyst (Fig. 5b) showed very minor peaks between 2 and 3 Å, which might be assigned to In-Pt bonds. However, the weak signal hindered further analysis due to the low concentration of In-Pt bonds in all In⁺ species arising from the Pt/In atomic ratio being close to 1:8. In contrast, Pt/In-Si-MFI and PtIn/SiO₂ catalysts only demonstrated a minor decrease in the In K-edge absorption intensity, with EXAFS spectra prominently featuring In₂O₃, suggesting that only a fraction of In was reduced due to the presence of Pt, while the majority remained as In₂O₃ nanoparticles. EXAFS fitting data (Supplementary Tables 1, 2, Supplementary Fig. 33-40) further corroborated these findings, revealing a decrease in the coordination number (CN) of In-O and the emergence of In-Pt bonds. For instance, in Pt/In-Si-MFI, the CN of In-O and In-O-In decreased from 5.6 ± 0.5 and 4.7 ± 0.9 in fresh sample to 4.8 ± 0.3 and 4.0 ± 0.5 in reduced sample, respectively, with a minor contribution potentially from the In-Pt bond (CN = 0.13 ± 0.06 , $d = 2.64 \pm 0.04$ nm). For PtIn/ SiO_2 , the CN of In-O and In-O-In decreased from 5.8 ± 0.6 and 5.1 ± 1.1 in fresh sample to 5.0 ± 0.2 and 4.1 ± 0.4 in reduced sample, respectively, but with a notable In-Pt bond (CN = 0.43 ± 0.05 , $d = 2.64 \pm 0.01$ nm). The more pronounced In-Pt coordination number in PtIn/SiO₂ compared to Pt/In-Si-MFI was attributed to the preparation of the former via a onestep impregnation method, which contrasted with the two-step procedures of the latter, resulting in a different extent of alloy formation.

Analysis of the Pt L_3 -edge XANES and EXAFS provided insights into Pt speciation within Ptln-based catalysts. After reduction, all Pt-containing samples demonstrated absorption features generally similar to the metallic phase, with notable differences upon detailed

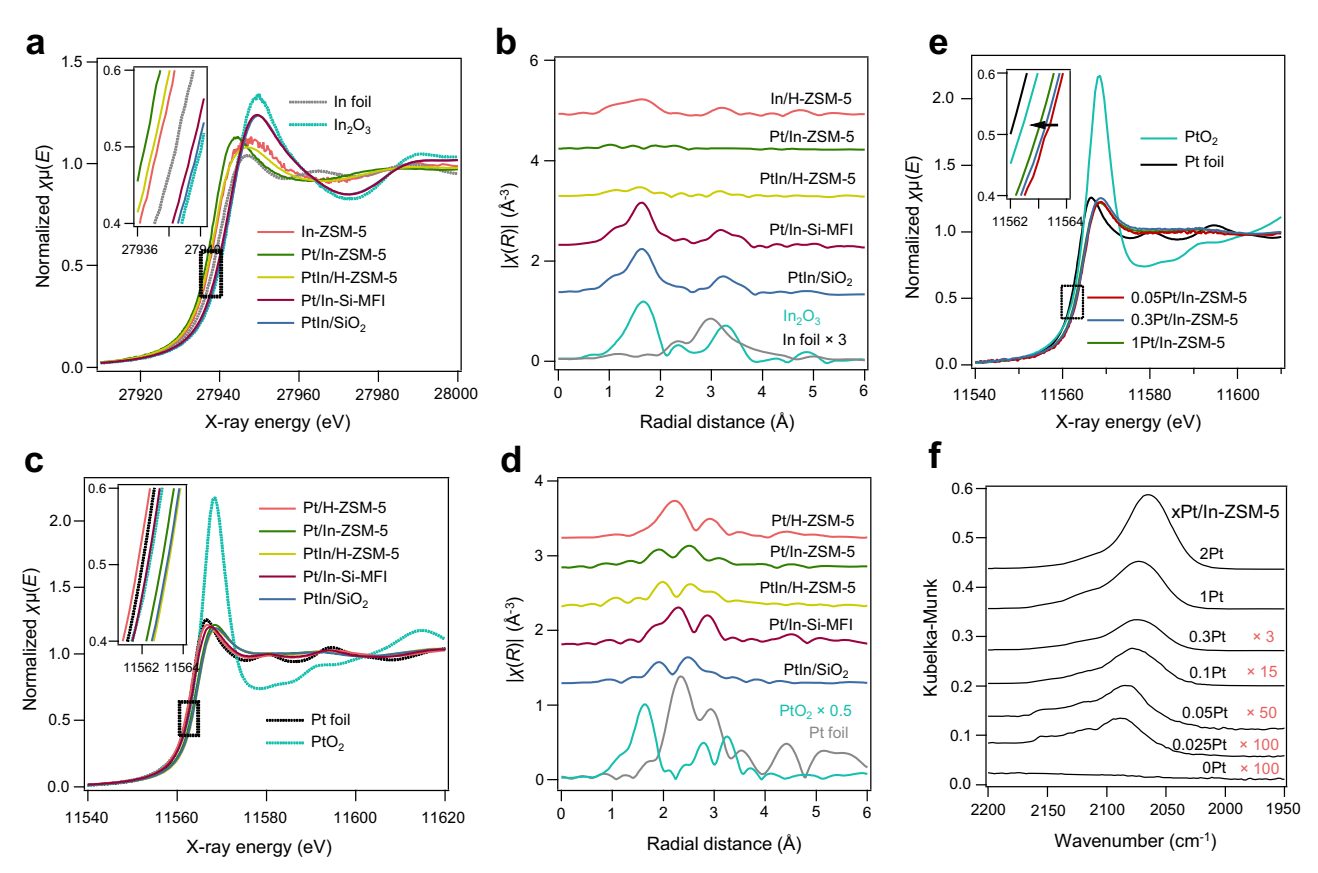


Fig. 5 | In-situ XANES, EXAFS, and CO-DRIFTS investigations over Pt/In-ZSM-5 catalysts. a In-situ XANES spectra of In K-edge and (b) in-situ Fourier-transformed EXAFS spectra over PtIn-based catalysts. In foil and In_2O_3 were also measured as standards for reference. c In-situ XANES spectra of Pt L_3 -edge and d in-situ Fourier-transformed EXAFS spectra over PtIn-based catalysts. e In-situ XANES spectra of Pt

 L_3 -edge over xPt/In-ZSM-5 catalysts. The spectra were collected in the presence of 20% H_2 /He at 550 °C. **f** CO-DRIFTS of xPt/In-ZSM-5 with different Pt loadings. The catalysts were reduced at 550 °C and then cooled down to room temperature in He gas before CO adsorption.

examination. For Pt/In-Si-MFI, the absorption was nearly identical to that of Pt/H-ZSM-5, indicative of Pt nanoparticles ~1.3 nm in size (CN(Pt-Pt) = 8.7). EXAFS fittings for reduced Pt/In-Si-MFI samples revealed a predominance of Pt-Pt bonds ($CN = 7.2 \pm 1.7$) over Pt-In bonds (CN = 1.0 ± 0.5). Conversely, PtIn/H-ZSM-5 and PtIn/SiO₂ displayed slightly higher absorption energies, suggesting primary PtIn alloy formation. This was corroborated by EXAFS fittings showing PtIn/H-ZSM-5 with $CN(Pt-Pt) = 4.0 \pm 1.0$ and $CN(Pt-In) = 3.5 \pm 0.8$, and $PtIn/SiO_2$ with $CN(Pt-Pt) = 2.7 \pm 0.5$ and $CN(Pt-In) = 3.4 \pm 0.4$, confirming that a onestep impregnation method favored PtIn alloy formation. The absorption energy of Pt/In-ZSM-5 fell between that of Pt/H-ZSM-5 and PtIn/SiO₂, indicating the interaction between Pt and In species without forming the bulk PtIn alloy. In addition, the absorption energy of Pt within xPt/In-ZSM-5 samples showed a gradual increase with decreasing Pt size from clusters to single atoms (Fig. 5e). This trend was rationalized by the electron transfer (from Pt to In) that occurred when Pt was introduced, resulting in a partially positive charge of Pt and a slight reduction in In. In larger Pt clusters, these positive charges were more evenly distributed, resulting in an average valence state closer to that of the metallic phase, EXAFS fitting of Pt/In-ZSM-5 showed CN(Pt-Pt) = 2.8 ± 0.6 and CN(Pt-In) = 1.6 ± 0.6 for reduced Pt/In-ZSM-5 sample. The ratio of CN(Pt-Pt) to CN(Pt-In) was also between that of the Pt/H-ZSM-5 and PtIn/SiO₂ samples, further demonstrating the presence of Pt-In bond, but without bulk PtIn alloys. The difference between Pt/In-ZSM-5 and PtIn/H-ZSM-5 catalysts were discussed in detail, as shown in Supplementary Fig. 41. Therefore, we identified the active center of Pt/In-ZSM-5 catalyst as a Pt₄In cluster, primarily due to two reasons: (1) In speciation predominantly existed as In⁺ in the Pt/In-ZSM-5 catalyst, as evidenced by in-situ XANES, EXAFS, and pyridine-FTIR results. These findings provided the guidance that the active centers should be Pt_xIn clusters. (2) The HAADF-STEM image of the spent catalyst showed a particle size of 0.7 nm. The total CN of Pt-Pt and Pt-In from the XAFS measurements was 4.4, which was in line with the coordination environments of the Density functional theory (DFT) model of a Pt₄In cluster composed of five atoms. It was important to note that, while a cluster of five atoms could be useful for DFT studies to investigate the effects of Pt coordination with In on adsorption and surface reactions, it might not necessarily replicate the precise structure of catalysts used in experiments. As reported previously, the local coordination was critical to control the catalytic activity of an active site⁵⁰. Although there were minor differences in the EXAFS fittings, possibly due to the lack of a standard Pt-In⁺ pathway in the zeolite, the collective evidence strongly supported the configuration of the active center as a Pt₄In cluster.

The CO-DRIFTS results provided additional evidence for the extent of interaction between Pt with In⁺ in the Pt/In-ZSM-5 catalysts. As shown in Fig. 5f and Supplementary Fig. 42, the lack of a CO adsorption band on reduced In-ZSM-5 implied the negligible interaction between CO and In⁺. 1Pt/H-ZSM-5 showed an intense peak at 2082 cm⁻¹, characteristic of linearly adsorbed CO on metallic Pt and consistent with the in-situ XANES results (Fig. 5)²⁴. Notably, Pt/In-ZSM-5 exhibited a CO peak at a slightly lower frequency than Pt/H-ZSM-5. The red shift in the CO frequency for Pt/In-ZSM-5 suggested a stronger CO adsorption on this catalyst due to the interaction between In and Pt, resulting in a more effective d-π back-donation from Pt to CO⁵¹ and consistent with in-situ XANES results in Fig. 5. A higher In/Al ratio exhibited more pronounced interaction of CO with Pt (Supplementary Fig. 42). With the decrease of Pt loading (Fig. 5f), a notable blue shift in the CO frequency signified a reduced interaction strength between Pt species and CO molecules, aligning with the emergence of isolated Pt atoms that interacted less strongly with CO19, consistent with the insitu XANES results that a more positively charged Pt was on single Pt atoms (Fig. 5e).

Integrating HAADF-STEM images, in-situ XANES and EXAFS characterizations and CO-DRIFTS results led to a comprehensive understanding of Pt/In-ZSM-5 catalysts. At a 1% Pt loading, Pt₄ clusters stabilized by In⁺ within the ZSM-5 zeolite, were predominant. However, reducing the Pt loading to 0.05% favored the formation of single Pt atoms. For these catalysts, In was found to exist primarily in a +1-oxidation state at extra-framework positions (Fig. 3c), playing a crucial role in stabilizing slightly positively charged Pt atoms. This interaction mechanism was notably distinct from that in conventional PtIn-based catalysts, where In typically existed in a +3 oxidation state or in a metallic form, forming PtIn alloys^{48,52}.

DFT investigations of reaction mechanisms

DFT calculations were performed to gain more insights into the structural characteristics of Pt/In-ZSM-5 catalysts. ZSM-5 was described by the periodic MFI framework (Supplementary Fig. 43). Pt₁/In₁-ZSM-5 and Pt₄/In₁-ZSM-5 models (Supplementary Figs. 44, 45) were used to describe the isolated single Pt atom and Pt cluster, respectively. In₁-ZSM-5, Pt₁-ZSM-5, and Pt₄-ZSM-5 models (Supplementary Figs. 46–48) were also included for comparison. DFT-calculated partial density of states (PDOS) revealed a slight decrease in the oxidation state of In with an increasing Pt atoms from 1 to 4, evidenced by the downshift of In 5 s and 5p valence states (Fig. 6a). This was consistent with the slight decrease in edge position observed in

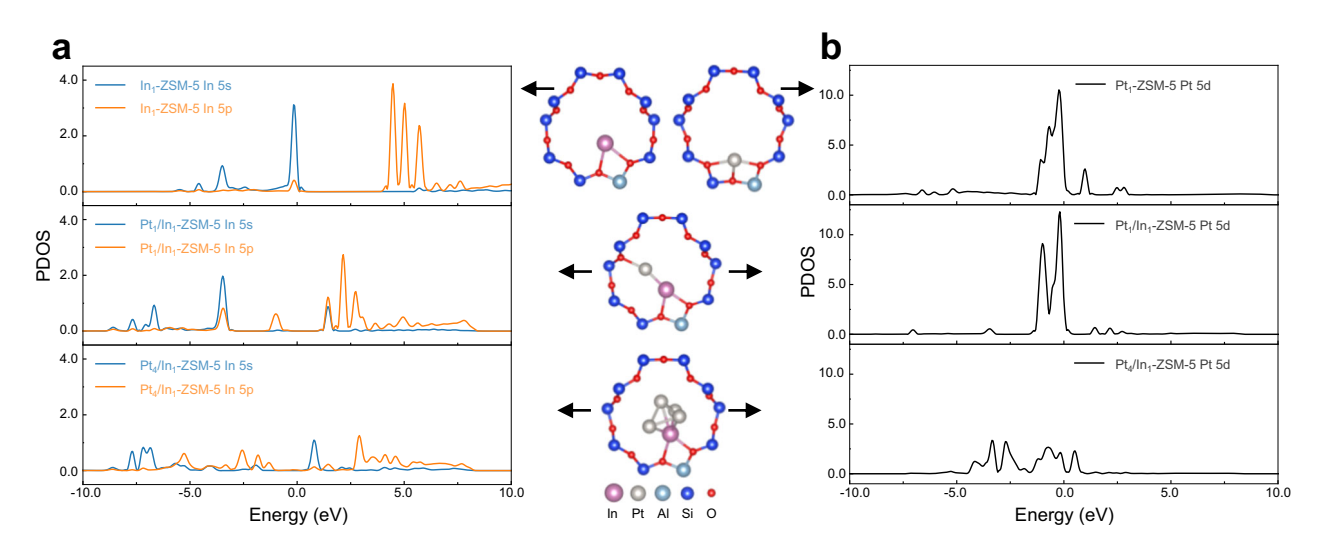


Fig. 6 | DFT-calculated PDOS for In and Pt orbitals. a In 5 s and 5p orbitals in In₁-ZSM-5, Pt₁/In₁-ZSM-5, and Pt₄/In₁-ZSM-5 models and (b) Pt 5d orbitals in Pt₁-ZSM-5, Pt₁/In₁-ZSM-5, and Pt₄/In₁-ZSM-5 models. Middle inset: optimized structures for In₁-ZSM-5, Pt₁-ZSM-5, Pt₁/In₁-ZSM-5, and Pt₄/In₁-ZSM-5.

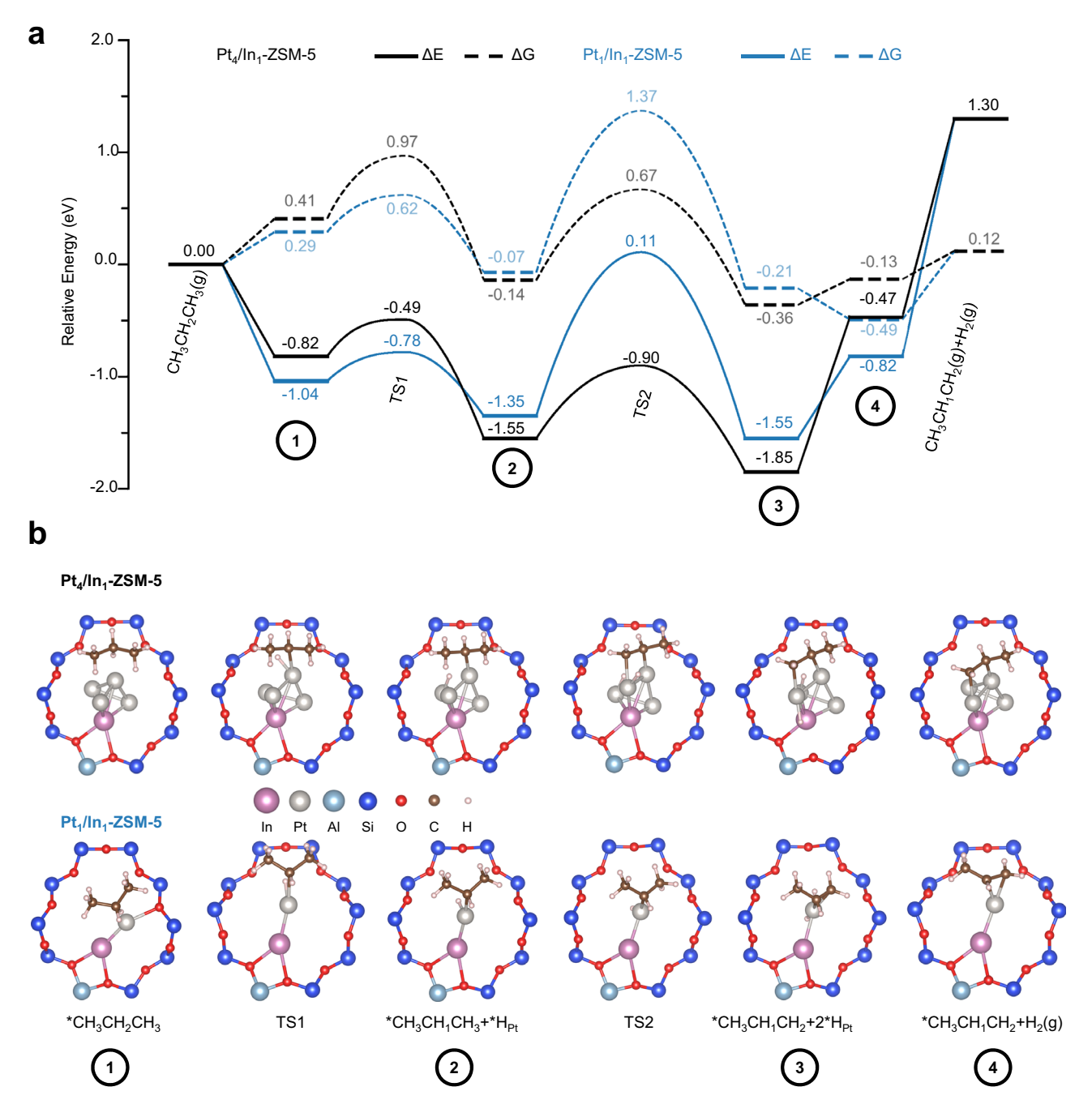


Fig. 7 | Reaction mechanism of propane dehydrogenation over Pt/In-ZSM-5 catalysts. a DFT-calculated potential energy diagram (solid line) and the Gibbs free energy diagram at 550 °C (dashed line) for the dehydrogenation of propane over Pt_I/In₁-ZSM-5 model and Pt₄/In₁-ZSM-5 model, also see Supplementary Table 4 for

reaction energy and activation energy of each elementary step. **b** DFT-optimized atomic structures for the reaction intermediates and transition states during PDH on Pt_1/In_1 -ZSM-5 model and Pt_4/In_1 -ZSM-5 models.

in-situ XANES (Fig. 5a). By comparison, on interaction with In, Pt of Pt_I/In_I-ZSM-5 was less positively charged than that of Pt_I-ZSM-5 by demonstrating a downshift of d-band, which eventually became more metallic with the increase of size to Pt₄/In_I-ZSM-5 (Fig. 6b). The formation of the Pt₄ cluster in ZSM-5 was more favorable than the formation of Pt₁ single atom, where the presence of In species could help stabilize Pt₁ and Pt₄ clusters compared to the case without the presence of In species in the ZSM-5 framework (Pt₄-ZSM-5: E_f = -8.59 eV; Pt₄/In_I-ZSM-5: E_f = -10.01 eV, Supplementary Fig. 49). These DFT results aligned with the structural characterizations obtained from insitu XAFS investigations and CO-DRIFTS results (Fig. 5), indicating that In⁺ in Pt/In-ZSM-5 effectively anchored Pt atom through direct Pt-In

interaction, with In being more positively charged than Pt. The differences in the electronic structure between Pt_I/In₁-ZSM-5 and Pt₄/In₁-ZSM-5 models should be responsible for the varied PDH performances.

The PDH mechanism was further explored using DFT for Pt_1/ln_1 -ZSM-5 and Pt_4/ln_1 -ZSM-5 (Fig. 7, Supplementary Fig. 50, 51, and Supplementary Tables 3, 4). As illustrated in Fig. 7a, the Pt cluster site of Pt_4/ln_1 -ZSM-5 (solid black line) was active toward the adsorption of $CH_3CH_2CH_3$ with an adsorption energy (E_{ads}) of -0.82 eV (Supplementary Fig. 50, Supplementary Table 3). The first C-H bond breaking of * $CH_3CH_2CH_3$ was preferred with a reaction energy (ΔE) of -0.73 eV and an activation energy (E_a) of 0.33 eV. The sequential C-H bond cleavage was also favorable ($\Delta E = -0.30$, $E_a = 0.60$ eV), where the reaction barrier

was lower than that on the Pt(111) surface $(E_a = ca. 0.7 \sim 1.1 \text{ eV})^{20,53,54}$. As a comparison, the single Pt atom site of Pt₁/In₁-ZSM-5 (Fig. 7a, solid blue) bounded CH₃CH₂CH₃ more strongly (Supplementary Fig. $E_{\text{ads}} = -1.04 \text{ eV}$). The cleavage of the first C-H bond of *CH₃CH₂CH₃ to *CH₃CH₁CH₃ was slightly less thermodynamically favorable but with a relatively lower barrier ($\Delta E = -0.31$, $E_a = 0.26$ eV), where a dissociated *H was coadsorbed at the same Pt₁ site. The sequential C-H bond cleavage resulted in the bindings of *CH₃CH₁CH₂ via a bidentate conformation together with two *H species at a Pt₁ site, which corresponded to a high barrier ($\Delta E = -0.20 \text{ eV}$, $E_a = 1.46 \text{ eV}$) due to the over-coordination of Pt₁. This step was much more difficult than that on Pt₄/In₁-ZSM-5. Alternatively, the second C-H bond scission could undergo a two-step path associated with the synergy between Pt₁ and neighboring In₁ (Supplementary Fig. 51, solid orange line). Specifically, the *H species on Pt hopped to the neighboring In site ($\Delta E = 0.92 \text{ eV}$), which was followed by the dehydrogenation of *CH₃CH₁CH₃ species to *CH₃CH₁CH₂ $(\Delta E = -0.55 \text{ eV}, E_a = 0.15 \text{ eV})$. However, the H-hopping process on Pt₁/In₁-ZSM-5 was still more difficult than the direct C-H bond breaking on Pt₄/ In₁-ZSM-5 model, and the corresponding barrier was too high to attribute to the experimentally observed high initial PDH rates (Fig. 3). Our DFT results indicated the superior advantage of the Pt₄ cluster site over single Pt atom site. By comparison, the hydrogen bonds provided by the ZSM-5 framework to stabilize the intermediates and transition states were rather limited and the contribution to tune the potential energies (Fig. 7b and Supplementary Fig. 51) was subtle.

To ensure the Pt₄ cluster rather than Pt₁ as the catalytic site that could enable active and selective dehydrogenation as observed experimentally (Fig. 3), the free energy was calculated by including the entropy contribution at 550 °C (Fig. 7a, dashed line). Indeed, Pt₄ cluster again displayed a lower apparent barrier of 0.97 eV than Pt₁ of 1.37 eV. Finally, as discussed above, the In₁-anchored Pt₁ site enabled the bidentate binding motif of *CH₃CH₁CH₂ with a strong adsorption energy (Supplementary Fig. 50, $E_{ads} = -2.12 \text{ eV}$), while In₁-anchored Pt₄ site provided a relatively weak binding of *CH₃CH₁CH₂ with two Pt atoms ($E_{ads} = -1.77$). Yet, the removal of *CH₃CH₁CH₂ was both feasible under the reaction temperature of 550 °C by lowering the adsorption energy to -0.61 eV for Pt₁/In₁-ZSM-5 and -0.25 eV for Pt₄/ In₁-ZSM-5 (Supplementary Fig. 50, Supplementary Table 3), which was much more favorable than the other steps involved in PDH for each case (Fig. 7b). This was further corroborated by the in-situ DRIFTS investigation (Supplementary Fig. 52) on the flow of propane over reduced Pt/In-ZSM-5. It showed that the C-H stretching band of propane disappeared rapidly upon being purged by He without the associated vibrational features of unsaturated hydrocarbons. In addition, in-situ XAFS investigations revealed that the oxidation states remained unchanged for both Pt and In, from the reduction stage to the reaction feed (Supplementary Fig. 53 and Supplementary Table 2), suggesting no appreciable hydrocarbon coverage at the active center formed upon reduction. Therefore, it was concluded that the desorption of *CH₃CH₁CH₂ was not a rate-limiting step, while the C-H scission, specifically the second C-H scission according to the DFT results, required the highest energy to overcome along the reaction pathway.

Without the presence of In species, the formation Pt₄ cluster in ZSM-5 was less preferred (Supplementary Fig. 49). This was consistent with the experimental observation that Pt clusters in the ZSM-5 framework were larger than those with the presence of In species (Supplementary Fig. 24). Upon exposure to propane, the first C-H bond breaking was not as favorable as Pt₄/In₁-ZSM-5 (Pt₄-ZSM-5: $\Delta E = -0.19$ eV; Pt₄/In₁-ZSM-5: $\Delta E = -0.73$ eV, in Supplementary Table 5). While the sequential dehydrogenation to propylene was more favorable for the Pt₄-ZSM-5 model (Pt₄-ZSM-5: $\Delta E = -1.17$ eV; Pt₄/In₁-ZSM-5: $\Delta E = -0.30$ eV). This was due to the more weakly anchored Pt₄ in Pt₄-ZSM-5 than that in Pt₄/In₁-ZSM-5, enabling structural fluxionality to selective bond-strengthening to propylene via the π-bond (Pt₄-ZSM-5: $E_b = -2.13$ eV;

Pt₄/In₁-ZSM-5: E_b = -1.77 eV in Supplementary Table 6, Supplementary Fig. 54). According to the calculated PDOS (Supplementary Fig. 55), the propylene adsorption introduced more significant change of Pt 5d states for Pt₄-ZSM-5 than Pt₄/In₁-ZSM-5. By comparison, the effect on the binding of *CH₃-CH₁-CH₃ via the σ-bond was much less (Pt₄-ZSM-5: E_b = -0.90 eV; Pt₄/In₁-ZSM-5: E_b = -0.82 eV in Supplementary Table 6, Supplementary Fig. 54).

Overall, the DFT calculations (Fig. 7) agreed well with the experimental observations (Figs. 2, 3) that Pt/In-ZSM-5 catalysts were active and selective for PDH. According to the DFT results, the superior dehydrogenation performance of Pt/In-ZSM-5 strongly depended on the size of Pt (single atom or clusters) anchored by In sites. Both the Pt₁ atom site and Pt₄ cluster site were active enough to enable facile propane adsorption and the first C-H bond cleavage (Fig. 7) by facilitating the electron transfer from Pt to the adsorbates, and moderately enough to allow the removal of the propylene product from the site under the reaction condition. While the situation to break the second C-H bond was rather different. It was hindered by over-coordination of the Pt₁ site of Pt₁/In₁-ZSM-5, but being facilitated by the direct participation of neighbored Pt atoms within of Pt₄/In₁-ZSM-5under hydrogenation conditions.

Discussion

A facile method has been developed to synthesize Pt clusters confined within In-modified ZSM-5 zeolites. This process involves initially creating In-ZSM-5 through a reductive solid-state ionexchange process, leading to the reduction of In₂O₃ and displacement of BAS, thereby forming stable extra-framework In⁺ cations within the ZSM-5 zeolite. Subsequent incorporation of Pt into In-ZSM-5 results in the formation of slightly positively charged Pt atoms stabilized by In⁺. The resulting Pt/In-ZSM-5 catalyst demonstrates excellent propane dehydrogenation performance at 550 °C, with propane conversion maintained at around 40% after 118 h and the propylene selectivity higher than 99.5%. Further characterizations reveal that the exceptional PDH performance is attributed to Pt clusters confined within the In-ZSM-5 zeolites. Low Pt loading (0.05%) results in a predominance of single Pt atoms within In-ZSM-5, which suffer from rapid deactivation despite high initial dehydrogenation rates. DFT calculations corroborate that the superior experimental performance is primarily due to Pt₄ clusters, which facilitate propane dehydrogenation and propylene desorption. To the best of our knowledge, this is the first time using In-modified commercial Al-containing zeolite to stabilize Pt clusters for PDH. The findings from this study open avenues for further catalytic applications of these readily available and easily synthesized catalysts.

Methods

Catalyst preparation

All reagents were used without purification. To obtain the parent H-ZSM-5 samples (Si/Al = 40), commercial NH₄-ZSM-5 samples (Alfa Aesar Si/Al = 40) were calcined in the air at 550 °C for 12 h at a heating rate of 2 °C·min⁻¹. The Si/Al ratios of the samples were determined to be 39.6 by X-ray fluorescence (XRF, Rigaku WDXRF). In/H-ZSM-5 was prepared by impregnating an aqueous solution of indium(III) nitrate hydrate (Sigma-Aldrich) into H-ZSM-5 zeolite through the IWI method, followed by drying at 80 °C and calcination at 550 °C in the air for 2 h with a ramp rate of 5 °C·min⁻¹. The calcined samples were denoted as In/H-ZSM-5(X, Y), where X and Y represented the Si/Al ratio and In/Al ratio, respectively. In-ZSM-5 samples were subsequently prepared via the reductive solid-state ion-exchange process, where In/H-ZSM-5 samples were reduced in 50 vol% H₂ in Ar at 550 °C for 1h with a heating rate of 10 °C·min⁻¹. Afterward, Pt was introduced on In-ZSM-5 by the same IWI method using an aqueous solution of tetraammineplatinum(II) nitrate (Sigma-Aldrich, 99.995% trace metals

basis), followed by drying at 80 °C and calcination at 350 °C in the air for 2 h with a ramp rate of $2 \, ^{\circ}\text{C-min}^{-1}$. The obtained products were denoted as xPt/In-ZSM-5, where x represented the Pt loadings. For the sake of brevity, In/H-ZSM-5 without parentheses referred to the sample with Si/Al and In/Al ratios of 40 and 1.0, which showed the same meaning as In/H-ZSM-5(40,1.0). Pt/In-ZSM-5 without x represented the Pt loading of 1 wt%. The XRF measurement of 1Pt/In-ZSM-5(40, 1.0) (same as Pt/In-ZSM-5) showed the Pt loading with 1.04% and In/Al ratio of 0.96, respectively, consistent with nominal loadings.

Ptln/H-ZSM-5 (1 wt% Pt and 4.5 wt% ln), Ptln/SiO₂(1:3) (1 wt% Pt and 1.7 wt% ln, with Pt/ln atom ratio of 1:3) and Ptln/SiO₂(1:8) (1 wt% Pt and 4.5 wt% ln, with Pt/ln atom ratio of 1:8) were prepared via a one-step IWI method using a mixed aqueous solution of indium(III) nitrate hydrate and tetraammineplatinum(II) nitrate. Note that Ptln/SiO₂(1:8) was in most cases abbreviated as Ptln/SiO₂. For comparison, In/SiO₂ (4.5 wt% ln), Pt/SiO₂ (1 wt% Pt), Pt/H-ZSM-5 (1 wt% Pt) were prepared by the same method with SiO₂ (Sigma-Aldrich, silica gel davisil, grade 646) and H-ZSM-5 zeolite, respectively. PtSn/SiO₂ (1 wt% Pt and 3 wt% Sn) and PtSn/ Al₂O₃ (1 wt% Pt and 3 wt%Sn) catalysts were prepared using IWI method with an aqueous solution of tetraammineplatinum(II) nitrate and SnCl₂·2H₂O (Sigma-Aldrich) on SiO₂ and γ -Al₂O₃ (Alfa Aesar, 99.97% metals basis), respectively. \ln_2 O₃ was purchased from Sigma-Aldrich (99.99% trace metals basis) and used as received.

In/Si-MFI (4.5 wt% In) was prepared by the same method using siliceous MFI that was synthesized by a hydrothermal method, as described in Supplementary Note 1. Pt/In-Si-MFI (1 wt% Pt) and Pt/In-ZSM-5(IE) (1 wt% Pt) were prepared using the two-step method used to prepare Pt/In-ZSM-5 catalyst: In/Si-MFI or In-ZSM-5(IE) was reduced at 550 °C, and then the Pt precursor was introduced.

Ga-ZSM-5, Co-ZSM-5, and Zn-ZSM-5, as well as their Pt-containing samples, were obtained via the same methodology as the preparation of Pt/In-ZSM-5 samples described above, except for the use of gallium(III) nitrate hydrate (Sigma-Aldrich) or cobalt(II) nitrate hexahydrate (Sigma-Aldrich) or zinc nitrate hydrate (Sigma-Aldrich) as the precursors.

Catalyst characterization

Elemental analysis was performed by XRF (Rigaku WDXRF). The H₂ temperature-programmed reduction (H2-TPR) profiles of the calcined catalysts were obtained using an AMI-300ip (Altamira) instrument equipped with a TCD detector. Typically, 100 mg of the catalyst was pretreated under He (50 mL min⁻¹) at 200 °C for 30 min and then cooled to 40 °C. The temperature-programmed reduction measurement was conducted in a mixture of 10% H₂/Ar (30 mL·min⁻¹) with a heating rate of 10 °C·min⁻¹ to 750 °C. The electron microscopy characterization of the catalysts was performed at the Center for Functional Nanomaterials, Brookhaven National Laboratory. Typically, the samples were ultrasonically dispersed in ethanol for 10 min. Afterward, a droplet was dripped onto a Lacey carbon film supported on a copper grid and fully dried before use. HAADF-STEM images were conducted with Hitachi HD 2700 C, and STEM-EDS were acquired on Themo-Fisher Talos F200X at an accelerating voltage of 200 kV to determine the particle size and element distribution of the catalysts, respectively. Other TEM images were collected at the JEOL 2100 F and JEOL 1400 instruments. The XRD measurements $(\lambda = 0.6199 \text{ Å})$ were collected at beamline 7-BM (QAS) of the National Synchrotron Light Source II (NSLS-II) at Brookhaven National Laboratory. Raman spectra for the spent catalysts were acquired using HORIBA Raman spectrometers and microscopes, employing a 532 nm laser source. The neutral density filter remained set at 25% of the laser power. Multiple spots were examined, and an average spectrum was generated. Raman spectra analysis was conducted using LabSpace 6 Spectroscopy Software. For the TPO analysis, ~20 mg of the spent catalyst was placed in a quartz tube. This was first dehydrated at 300 °C for 30 min under a He flow of 45 mL·min⁻¹, then cooled to 50 °C. Subsequently, a gas mixture of 20 vol% O₂/He (45 mL·min⁻¹) was introduced. The temperature was then increased to 800 °C at a ramp rate of 10 °C·min⁻¹. The analysis monitored atomic mass units (amu) for the following gases: 4 (He), 32 (O₂), 44 (CO₂). TGA was performed on a Pyris Series-Diamond TG/DTA instrument under oxygen flow (200 mL·min⁻¹) with temperature ramping (10 °C·min⁻¹) to 800 °C.

Pyridine-FTIR spectroscopy was conducted to identify the presence of BASs and LASs using an Agilent CARY 660 spectrometer with an MCT detector⁴². For sample preparation, ~20 mg of the catalyst powder was pressed into a wafer with a diameter of 1/2 inch, which was then vertically placed in a customized transmission cell. This cell was equipped with a vacuum manifold connected to a mechanical pump and a diffusion pump, achieving a vacuum level below 0.01 mTorr. In addition, the cell was wrapped with heating tapes and the temperature was controlled by a PID system with a thermocouple near the sample. Typically, the sample underwent dehydration at 550 °C for 30 min under vacuum to remove adsorbed molecules. Following this, H2 was introduced at 550 °C for 10 min and then evacuated. This reduction step was repeated three times to ensure thorough reduction. The sample was then cooled to 150 °C under vacuum. Excess pyridine was introduced into the transmission cell and subsequently evacuated; a process repeated three times to ensure full saturation of pyridine. A final evacuation for 15 min removed physisorbed pyridine before spectra collection. The spectra were obtained from 128 co-added scans with a resolution of 2 cm⁻¹, and normalized to the Si-O-Si bands between 1700 and 2000 cm⁻¹ for zeolite samples⁴².

CO diffuse reflectance infrared Fourier transform spectroscopy (CO-DRIFTS) experiments were performed on a Nicolet 6700 instrument equipped with a Harrick drifts cell at ambient pressure. Typically, the sample was heated to 550 °C in He (50 mL·min $^{-1}$), followed by the reduction in 10 vol% H $_2$ /He (50 mL·min $^{-1}$ in total) at the same temperature for 60 min. Next, the flow was switched to pure He to purge the sample for 10 min, then the sample was cooled down to room temperature in the flow of pure He. After that, the sample was treated with a 10 vol% CO/He (50 mL·min $^{-1}$ in total) for 30 min and then purged with pure He for 15 min, before collecting the spectrum. Note that the background spectrum was collected before flowing CO/He flow. In-situ $\rm H_2$ -D $_2$ exchange and propane dehydrogenation measurements were performed at 550 °C. The gas line was purged by pure He for 10 min before introducing the target gas.

The in-situ XAFS spectra of the Pt L₃-edge and In K-edge were collected at beamline 7-BM (QAS) of the National Synchrotron Light Source II (NSLS-II) at Brookhaven National Laboratory. For each measurement, an appropriate amount of the catalyst was compressed into a wafer (1/2 in.) before being loaded into a Nashner-Adler reaction cell sealed by Kapton windows, which allowed for the simultaneous collection of both the transmission and fluorescence signals. The sample was first reduced under an H₂/ He flow (25 mL·min⁻¹) at 550 °C for 30 min, followed by the introduction of 20 vol% C₃H₈ in He flow at the same temperature. The exsitu XAFS spectra of the Pt L₃-edge and In K-edge were collected at ambient conditions. For each measurement, the catalyst was pressed and sealed with Kapton tape. The XAFS spectra were collected simultaneously via transmission and fluorescence modes. Data processing was preformed using the Athena and Artemis software, parts of the Demeter package⁵⁵.

Propane dehydrogenation performance measurements

Catalytic reaction rates were measured using a fixed bed plug flow reactor, consisting of a quartz glass tube (1/2 in. in diameter). The catalyst bed typically contained 100 mg of the catalyst with a particle size range of 40–60 mesh. A thermocouple was placed close to the catalyst bed to ensure accurate temperature measurement. Before the propane dehydrogenation tests, the catalyst was heated

to $550\,^{\circ}\text{C}$ (or $580\,^{\circ}\text{C}$) or $600\,^{\circ}\text{C}$) for $60\,^{\circ}\text{min}$ with a ramp rate of $10\,^{\circ}\text{C}\cdot\text{min}^{-1}$ in $50\,^{\circ}\text{C}$ ML-min⁻¹), followed by purging with Ar at the same temperature for another $10\,^{\circ}\text{min}$. The reduced sample was then exposed to $20\,^{\circ}\text{C}$ MB in Ar or pure C_3H_8 flow with the total pressure maintained at atmospheric pressure. The reactor effluent was periodically injected into an online gas chromatograph (GC) (Agilent 7890B), using a heated gas line. The GC was equipped with a Plot Q and MOLESEIVE column and a thermal conductivity detector (TCD) and flame ionization detector (FID) used for gas analysis. TCD and FID response factors for Ar, CH₄, C_2H_4 , C_3H_6 , and C_3H_8 were calibrated before the product analysis. The conversion of propane was calculated using Eq. 1, and the selectivity and yield of CH₄, C_2H_4 , and C_3H_6 were determined using Eqs. 2 and 3, and the carbon balance was obtained using Eq. 4.

$$C_3 H_8 conversion = \left(1 - \frac{F_{C_3 H_{8, outlet}}}{F_{C_3 H_{8, inlet}}}\right) \times 100\%$$
 (1)

Selectivity =
$$\frac{n_i \times F_{i, \text{ outlet}}}{\sum n_i \times F_{i, \text{ outlet}}} \times 100\%$$
 (2)

$$Yield = \frac{n_i \times F_{i,outlet}}{3 \times F_{C_3} H_{g_{inlet}}} \times 100\%$$
 (3)

Carbon balance =
$$\frac{3 \times F_{C_3 H_{8, \text{outlet}}} + \sum_{i} n_i \times F_{i, \text{outlet}}}{3 \times F_{C_3 H_{8, \text{inlet}}}} \times 100\%$$
 (4)

where i represents the propane dehydrogenation products CH₄, C₂H₄, C₃H₆ in the effluent gas, n_i is the number of carbon atoms of component i, and F_i is the molar flow rate.

Similar methods were used to show the ethane dehydrogenation performance, as shown in Eqs. 5–7.

$$C_2H_6$$
 conversion = $\left(1 - \frac{F_{C_2H_{6, outlet}}}{F_{C_2H_{6, inlet}}}\right) \times 100\%$ (5)

$$C_2H_4 \text{ selectivity} = \frac{2 \times F_{C_2H_{4, \text{ outlet}}}}{F_{\text{CH4, outlet}} + 2 \times F_{C_2H_{4, \text{ outlet}}}} \times 100\%$$
 (6)

Carbon balance =
$$\frac{F_{\text{CH}_{4,\text{outlet}}} + 2 \times F_{\text{C}_2\text{H}_{4,\text{outlet}}} + 2 \times F_{\text{C}_2\text{H}_{6,\text{outlet}}}}{2 \times F_{\text{C}_2\text{H}_{6,\text{inlet}}}} \times 100\% \quad (7)$$

The deactivation coefficient was calculated by Eq. 8²⁴.

$$k_{d} = \frac{\ln\left(\frac{1 - X_{C_{3}H_{8}}}{X_{C_{3}H_{8}}}\right) - \ln\left(\frac{1 - X_{C_{3}H_{8}}^{2}}{X_{C_{3}H_{8}}^{0}}\right)}{t}$$
(8)

where, $X_{C_3H_8}^0$ and $X_{C_3H_8}$ represented the initial propane conversion and propane conversion at t, respectively.

DFT calculations

Spin-polarized DFT^{56,57} calculations were performed based on Vienna ab initio simulation package⁵⁸. The projector augmented wave method^{59,60} together with GGA exchange-correlation functional plus the PBE functional⁶¹ and DFT-D3 method of Grimme with zero-damping function⁶² were employed with a 500 eV kinetic energy cut-off. The Γ -point⁶³ was applied for all the calculations and the Gaussian smearing with width 0.05 eV was used to improve the convergence. The criteria for total energies and forces on all atoms were set as

 $10^{-5}\,\text{eV}$ and $0.03\,\text{eV}\,\text{Å}^{-1}$ for convergence, respectively. The climbing nudged elastic band method 64 were conducted to obtain the transition states with nine configurations generated between the initial and final states

The adsorption energy of adsorbate on the surface was calculated as:

$$E_{ads} = E(Adsorbate/Surface) - E(Surface) - E(Adsorbate)$$
 (9)

where E is the total energy (E_{DFT}) obtained from DFT calculations with zero-point energy (ZPE) correction, E_{ZPE} :

$$E_{ZPE} = \sum_{i}^{number\ of\ modes} \frac{1}{2} h v_i \tag{10}$$

where v_i is DFT calculated harmonic vibrational frequency, h is the Planck constant.

Gibbs free energies at the specific temperature (T) were calculated based on the following equation^{65,66}:

$$G(T) = E_{DFT} + E_{ZPF} - T \times S(T) \tag{11}$$

The entropies for gas phase molecules (propane, propylene and hydrogen) were taken from NIST Chemistry WebBook⁶⁷. The entropies for all the intermediates and transition states involved were calculated based on the following equation⁶⁸:

$$S = R \sum_{i=1}^{number of modes} \left\{ \frac{hv_i/k_B T}{\exp(hv_i/k_B T) - 1} - \ln[1 - \exp(-hv_i/k_B T)] \right\}$$
(12)

Where R and k_B are the gas phase constant and the Boltzmann constant, respectively.

The ZSM-5 zeolite was modeled based on the periodic MFI framework (Supplementary Fig. 43) taken from the Database of Zeolite Structures 69 . The DFT-optimized MFI unit cell has a lattice constant of 20.26 Å \times 19.92 Å \times 13.37 Å, which are consistent with the experimental determined values (20.07 Å \times 19.92 Å \times 13.42 Å) 70 . One Si atom at the T7 site, which has been identified as the preferred framework site for Aluminum substitution 71 , was replaced by one Al in this work to anchor the active metal species.

The formation energy for $M_xM'_y$ -ZSM-5 zeolite models (M, M': Pt, In) was calculated as:

$$E_f = E(M_x M'_y - ZSM - 5) - E(M_x) - E(M'_y) - E(ZSM - 5)$$
 (13)

Data availability

All the data that support the findings of this study are available within the paper and supplementary information file, or from the corresponding author on reasonable request. The structures of DFT calculations are provided within this paper.

References

- Liu, L. & Corma, A. Metal catalysts for heterogeneous catalysis: from single atoms to nanoclusters and nanoparticles. *Chem. Rev.* 118, 4981–5079 (2018).
- Dong, C. et al. Fully exposed palladium cluster catalysts enable hydrogen production from nitrogen heterocycles. *Nat. Catal.* 5, 485–493 (2022).
- Zhang, K. et al. Generation of subnanometer metal clusters in silicoaluminate zeolites as bifunctional catalysts. JACS Au 3, 3213–3226 (2023).

- Sattler, J. J. H. B., Ruiz-Martinez, J., Santillan-Jimenez, E. & Weckhuysen, B. M. Catalytic dehydrogenation of light alkanes on metals and metal oxides. *Chem. Rev.* 114. 10613–10653 (2014).
- Ma, Y. et al. Germanium-enriched double-four-membered-ring units inducing zeolite-confined subnanometric Pt clusters for efficient propane dehydrogenation. Nat. Catal. 6, 506–518 (2023).
- Qi, L. et al. Propane dehydrogenation catalyzed by isolated Pt atoms in ≡SiOZn-OH nests in dealuminated zeolite Beta. J. Am. Chem. Soc. 143, 21364-21378 (2021).
- Qi, L. et al. Dehydrogenation of propane and n-butane catalyzed by isolated PtZn₄ sites supported on self-pillared zeolite pentasil nanosheets. ACS Catal. 12, 11177–11189 (2022).
- Chang, X. et al. Designing single-site alloy catalysts using a degreeof-isolation descriptor. Nat. Nanotechnol. 18, 611–616 (2023).
- Yan, W., Sun, Q. & Yu, J. Dehydrogenation of propane marches on. Matter 4, 2642–2644 (2021).
- Sun, M.-L., Hu, Z.-P., Wang, H.-Y., Suo, Y.-J. & Yuan, Z.-Y. Design strategies of stable catalysts for propane dehydrogenation to propylene. ACS Catal. 13, 4719–4741 (2023).
- Chen, S. et al. Propane dehydrogenation: catalyst development, new chemistry, and emerging technologies. *Chem. Soc. Rev.* 50, 3315–3354 (2021).
- 12. Li, X., Pei, C. & Gong, J. Shale gas revolution: Catalytic conversion of C_1 – C_3 light alkanes to value-added chemicals. *Chem* **7**, 1755–1801 (2021).
- 13. Chernyak, S. A. et al. olefin synthesis from a diversity of renewable and fossil feedstocks: state-of the-art and outlook. *Chem. Soc. Rev.* **51**, 7994–8044 (2022).
- Carter, J. H. et al. Direct and oxidative dehydrogenation of propane: from catalyst design to industrial application. *Green. Chem.* 23, 9747–9799 (2021).
- Chen, C. et al. Nature of active phase of VO catalysts supported on SiBeta for direct dehydrogenation of propane to propylene. Chin. J. Catal. 41, 276–285 (2020).
- Zhang, Y. et al. Control of coordinatively unsaturated Zr sites in ZrO₂ for efficient C-H bond activation. Nat. Commun. 9, 3794 (2018).
- Otroshchenko, T., Kondratenko, V. A., Rodemerck, U., Linke, D. & Kondratenko, E. V. ZrO₂-based unconventional catalysts for nonoxidative propane dehydrogenation: factors determining catalytic activity. J. Catal. 348, 282–290 (2017).
- Yuan, Y., Zhao, Z., Lobo, R. F. & Xu, B. Site diversity and mechanism of metal-exchanged zeolite catalyzed non-oxidative propane dehydrogenation. Adv. Sci. 10, 2207756 (2023).
- Zhang, W. et al. Size dependence of pt catalysts for propane dehydrogenation: from atomically dispersed to nanoparticles. ACS Catal. 10, 12932–12942 (2020).
- Zhai, P. et al. CO₂-mediated oxidative dehydrogenation of propane enabled by Pt-based bimetallic catalysts. Chem 9, 3268–3285 (2023).
- Searles, K. et al. Highly productive propane dehydrogenation catalyst using silica-supported Ga–Pt nanoparticles generated from single-sites. J. Am. Chem. Soc. 140, 11674–11679 (2018).
- Nakaya, Y., Hirayama, J., Yamazoe, S., Shimizu, K. & Furukawa, S. Single-atom Pt in intermetallics as an ultrastable and selective catalyst for propane dehydrogenation. *Nat. Commun.* 11, 2838 (2020).
- Nakaya, Y., Xing, F., Ham, H., Shimizu, K. & Furukawa, S. Doubly decorated platinum–gallium intermetallics as stable catalysts for propane dehydrogenation. *Angew. Chem. Int. Ed.* 60, 19715–19719 (2021).
- Motagamwala, A. H., Almallahi, R., Wortman, J., Igenegbai, V. O. & Linic, S. Stable and selective catalysts for propane dehydrogenation operating at thermodynamic limit. Science 373, 217–222 (2021).
- 25. Chen, S. et al. Propane dehydrogenation on single-site [PtZn₄] intermetallic catalysts. *Chem* **7**, 387–405 (2021).

- Sun, G. et al. Breaking the scaling relationship via thermally stable Pt/Cu single atom alloys for catalytic dehydrogenation. *Nat. Commun.* 9, 4454 (2018).
- Sun, Q. et al. Subnanometer bimetallic platinum-zinc clusters in zeolites for propane dehydrogenation. *Angew. Chem., Int. Ed.* 59, 19450-19459 (2020).
- Liu, L. et al. Regioselective generation and reactivity control of subnanometric platinum clusters in zeolites for high-temperature catalysis. *Nat. Mater.* 18, 866–873 (2019).
- Liu, L. et al. Structural modulation and direct measurement of subnanometric bimetallic PtSn clusters confined in zeolites. *Nat. Catal.* 3, 628–638 (2020).
- Ryoo, R. et al. Rare-earth-platinum alloy nanoparticles in mesoporous zeolite for catalysis. *Nature* 585, 221–224 (2020).
- Bhan, A. & Iglesia, E. A link between reactivity and local structure in acid catalysis on zeolites. Acc. Chem. Res. 41, 559–567 (2008).
- Yan, P. et al. Facile and eco-friendly approach to produce confined metal cluster. Catalysts J. Am. Chem. Soc. 145, 9718–9728 (2023).
- 33. Zhu, H. et al. Migration-agglomeration-lockup of metal particles in zeolite for ultra-stable propane dehydrogenation catalysts. Preprint at https://doi.org/10.21203/rs.3.rs-2231668/v1 (2022).
- Zeng, L. et al. Stable anchoring of single rhodium atoms by indium in zeolite alkane dehydrogenation catalysts. *Science* 383, 998–1004 (2024).
- Phadke, N. M., Mansoor, E., Bondil, M., Head-Gordon, M. & Bell, A. T. Mechanism and kinetics of propane dehydrogenation and cracking over Ga/H-MFI prepared via vapor-phase exchange of H-MFI with GaCl₃. J. Am. Chem. Soc. 141, 1614–1627 (2019).
- 36. Yuan, Y., Lee, J. S. & Lobo, R. F. Ga*-chabazite zeolite: a highly selective catalyst for nonoxidative propane dehydrogenation. *J. Am. Chem.* Soc. **144**, 15079–15092 (2022).
- 37. Schreiber, M. W. et al. Lewis-Brønsted acid pairs in Ga/H-ZSM-5 To catalyze dehydrogenation of light alkanes. *J. Am. Chem.* Soc. **140**, 4849–4859 (2018).
- 38. Yuan, Y., Brady, C., Lobo, R. F. & Xu, B. Understanding the correlation between Ga speciation and propane dehydrogenation activity on Ga/H-ZSM-5 catalysts. ACS Catal. 11, 10647–10659 (2021).
- 39. Yuan, Y. & Lobo, R. F. Zinc speciation and propane dehydrogenation in Zn/H-ZSM-5 catalysts. ACS Catal. 13, 4971–4984 (2023).
- Yuan, Y. & Lobo, R. F. Propane dehydrogenation over extraframework In(i) in chabazite zeolites. *Chem. Sci.* 13, 2954–2964 (2022).
- 41. Maeno, Z. et al. Isolated indium hydrides in CHA zeolites: speciation and catalysis for nonoxidative dehydrogenation of ethane. *J. Am. Chem.* Soc. **142**, 4820–4832 (2020).
- Yuan, Y., Brady, C., Annamalai, L., Lobo, R. F. & Xu, B. Ga speciation in Ga/H-ZSM-5 by in-situ transmission FTIR spectroscopy. *J. Catal.* 393, 60–69 (2021).
- Phadke, N. M. et al. Characterization of isolated Ga³⁺ cations in Ga/ H-MFI prepared by vapor-phase exchange of H-MFI zeolite with GaCl₃. ACS Catal. 8, 6106–6126 (2018).
- Meitzner, G. D., Iglesia, E., Baumgartner, J. E. & Huang, E. S. The chemical state of gallium in working alkane dehydrocyclodimerization catalysts. In situ gallium K-edge X-ray absorption spectroscopy. J. Catal. 140, 209–225 (1993).
- Getsoian, A. Organometallic model complexes elucidate the active gallium species in alkane dehydrogenation catalysts based on ligand effects in Ga K-edge XANES. Catal. Sci. Technol. 6, 6339–6353 (2016).
- Li, L., Chalmers, J. A., Bare, S. R., Scott, S. L. & Vila, F. D. Rigorous oxidation state assignments for supported Ga-containing catalysts using theory-informed X-ray absorption spectroscopy signatures from well-defined Ga(I) and Ga(III) compounds. ACS Catal. 13, 6549–6561 (2023).

- Rochlitz, L. et al. Silica-supported, narrowly distributed, subnanometric Pt–Zn particles from single sites with high propane dehydrogenation performance. *Chem. Sci.* 11, 1549–1555 (2020).
- Zhou, J. et al. Potassium-promoted Pt-In bimetallic clusters encapsulated in silicalite-1 zeolite for efficient propane dehydrogenation. Chem. Eng. J. 455, 139794 (2022).
- Xu, Z., Yue, Y., Bao, X., Xie, Z. & Zhu, H. Propane dehydrogenation over Pt clusters localized at the Sn single-site in zeolite framework. ACS Catal. 10, 818–828 (2020).
- Calle-Vallejo, F. et al. Finding optimal surface sites on heterogeneous catalysts by counting nearest neighbors. Science 350, 185–189 (2015).
- Zhang, X., Cui, G. & Wei, M. Ptln Alloy Catalysts toward Selective Hydrogenolysis of Glycerol to 1,2-Propanediol. *Ind. Eng. Chem. Res.* 59, 12999–13006 (2020).
- Deng, L., Chen, Q., Jiang, X., Liu, X. & Wang, Z. Effect of In addition on the performance of a Pt-In/SBA-15 catalyst for propane dehydrogenation. Catal. Today 410, 175–183 (2023).
- 53. Yang, M.-L., Zhu, Y.-A., Zhou, X.-G., Sui, Z.-J. & Chen, D. First-principles calculations of propane dehydrogenation over PtSn catalysts. ACS Catal. 2, 1247–1258 (2012).
- Sun, S., Sun, G., Pei, C., Zhao, Z.-J. & Gong, J. Origin of performances of Pt/Cu single-atom alloy catalysts for propane dehydrogenation. J. Phys. Chem. C 125, 18708–18716 (2021).
- Ravel, B. & Newville, M. ATHENA, ARTEMIS, HEPHAESTUS: data analysis for X-ray absorption spectroscopy using IFEFFIT. J. Synchrotron. Rad 12, 537–541 (2005).
- Hohenberg, P. & Kohn, W. Inhomogeneous electron gas. *Phys. Rev.* 136, B864–B871 (1964).
- Kohn, W. & Sham, L. J. Self-consistent equations including exchange and correlation effects. *Phys. Rev.* **140**, A1133–A1138 (1965).
- 58. Kresse, G. & Furthmüller, J. Efficient iterative schemes for ab initio total-energy calculations using a plane-wave basis set. *Phys. Rev. B* **54**, 11169–11186 (1996).
- Blöchl, P. E. Projector augmented-wave method. *Phys. Rev. B* 50, 17953–11979 (1994).
- Kresse, G. & Joubert, D. From ultrasoft pseudopotentials to the projector augmented-wave method. Phys. Rev. B 59, 1758–1775 (1999).
- 61. Perdew, J. P., Burke, K. & Ernzerhof, M. Generalized gradient approximation made simple. *Phys. Rev. Lett.* **77**, 3865–3868 (1996).
- Grimme, S., Antony, J., Ehrlich, S. & Krieg, H. A consistent and accurate ab initio parametrization of density functional dispersion correction (DFT-D) for the 94 elements H-Pu. Chem. Phys. 132, 154104 (2010).
- 63. Monkhorst, H. J. & Pack, J. D. Special points for Brillouin-zone integrations. *Phys. Rev. B* **13**, 5188–5192 (1976).
- Henkelman, G. & Jónsson, H. Improved tangent estimate in the nudged elastic band method for finding minimum energy paths and saddle points. Chem. Phys. 113, 9978–9985 (2000).
- Gomez, E., Nie, X., Lee, J. H., Xie, Z. & Chen, J. G. Tandem reactions of CO₂ reduction and ethane aromatization. *J. Am. Chem. Soc.* 141, 17771–17782 (2019).
- Xie, Z. et al. Catalytic tandem CO₂-ethane reactions and hydroformylation for C3 oxygenate production. ACS Catal. 12, 8279–8290 (2022).
- 67. Linstrom, P. J. & Mallard, W. G. NIST standard reference database number 69, National Institute of Standards and Technology: Gaithersburg MD, 20899. https://doi.org/10.18434/T4D303 (accessed September 2022) (2011).
- Gokhale, A. A., Kandoi, S., Greeley, J. P., Mavrikakis, M. & Dumesic, J. A. Molecular-level descriptions of surface chemistry in kinetic models using density functional theory. *Chem. Eng. Sci.* 59, 4679–4691 (2004).

- Baerlocher, C. & McCusker, L. B. Database of Zeolite Structures. http://www.iza-structure.org/databases/. (accessed September 2022).
- Olson, D. H., Kokotailo, G. T., Lawton, S. L. & Meier, W. M. Crystal structure and structure-related properties of ZSM-5. *J. Phys. Chem.* 85, 2238–2243 (1981).
- Kim, C. W., Heo, N. H. & Seff, K. Framework sites preferred by aluminum in zeolite ZSM-5. Structure of a fully dehydrated, fully Cs⁺exchanged ZSM-5 crystal (MFI, Si/Al= 24). J. Phys. Chem. C. 115, 24823–24838 (2011).

Acknowledgements

This work was financially supported by the US Department of Energy, Office of Basic Energy Sciences, Division of Chemical Sciences, Geosciences, & Biosciences, Catalysis Science Program under contract DE-SC0012704. This research used resources from the Center for Functional Nanomaterials (CFN) and beamline 7-BM (QAS) of the National Synchrotron Light Source II (NSLS-II) at Brookhaven National Laboratory (Contract Nos. DE-SC0012704 and DE-SC0012653). Beamline operations were supported in part by the Synchrotron Catalysis Consortium (U.S. DOE, Office of Basic Energy Sciences, Grant No. DE-SC0012335). We acknowledged Prof. Raul F. Lobo for providing the instrument for the pyridine-FTIR measurements, and the assistance of Dr. Nebojsa Marinkovic, Dr. Zhenhua Xie, and Dr. Zhexi Lin during the XAFS measurements. All the theoretical calculations were conducted using computational resources at the Center for Functional Nanomaterials (CFN), and the Scientific Data and Computing Center, a component of the Computational Science Initiative, at BNL under Contract No. DE-SC0012704 and at the National Energy Research Scientific Computing Center (NERSC), a DOE Office of Science User Facility, supported by the Office of Science of the DOE under contract DE-AC02-05CH11231.

Author contributions

Y.Y. and J.G.C. conceived the idea and designed the experiments; Y.Y. carried out catalyst synthesis, characterization, catalytic performance and analyzed all experimental data, and wrote the first draft of the paper; S.H. conducted the HADDF-STEM images and EDS elemental mapping images. E.H. performed the DFT calculations, DFT data analysis, and contributed to the first draft under the guidance of J.G.C. and P.L. All authors have reviewed and edited the paper, and approved the final version of the manuscript.

Competing interests

The authors declare no competing interests.

Additional information

Supplementary information The online version contains supplementary material available at https://doi.org/10.1038/s41467-024-50709-y.

Correspondence and requests for materials should be addressed to Ping Liu or Jingguang G. Chen.

Peer review information *Nature Communications* thanks De Chen, and the other, anonymous, reviewer(s) for their contribution to the peer review of this work. A peer review file is available.

Reprints and permissions information is available at http://www.nature.com/reprints

Publisher's note Springer Nature remains neutral with regard to jurisdictional claims in published maps and institutional affiliations.

Open Access This article is licensed under a Creative Commons Attribution-NonCommercial-NoDerivatives 4.0 International License, which permits any non-commercial use, sharing, distribution and reproduction in any medium or format, as long as you give appropriate credit to the original author(s) and the source, provide a link to the Creative Commons licence, and indicate if you modified the licensed material. You do not have permission under this licence to share adapted material derived from this article or parts of it. The images or other third party material in this article are included in the article's Creative Commons licence, unless indicated otherwise in a credit line to the material. If material is not included in the article's Creative Commons licence and your intended use is not permitted by statutory regulation or exceeds the permitted use, you will need to obtain permission directly from the copyright holder. To view a copy of this licence, visit https://creativecommons.org/licenses/by-nc-nd/4.0/.

© The Author(s) 2024